

1 **Eruption of Kimberlite Magmas: Physical volcanology, Geomorphology, and Age**  
2 **of the Youngest Kimberlitic Volcanoes known on Earth (the Upper**  
3 **Pleistocene/Holocene Igwisi Hills volcanoes, Tanzania)**  
4

5 Richard J. Brown<sup>1\*</sup>, S. Many<sup>2</sup>, I. Buisman<sup>3</sup>, G. Fontana<sup>4</sup>, M. Field<sup>5</sup>, C. Mac Niocaill<sup>4</sup>, R.S.J. Sparks<sup>6</sup>,  
6 F.M. Stuart<sup>7</sup>  
7

8 <sup>1</sup>Department of Earth and Environmental Sciences, Open University, Walton Hall, Milton Keynes  
9 MK7 6AA, UK

10 <sup>2</sup>Department of Geology, University of Dar es Salaam, Dar es Salaam, Tanzania

11 <sup>3</sup>Department of Earth Sciences, University of Cambridge, Downing Street, Cambridge, CB2 3EQ, UK

12 <sup>4</sup>Department of Earth Sciences, University of Oxford, Parks Road, Oxford OX1 3PR, UK

13 <sup>5</sup>AMEC plc, Environment & Infrastructure - Growth Regions (Mining Services Group)

14 International House, Dover Place, Ashford, TN23 1HU

15 <sup>6</sup>Department of Earth Sciences, Wills Memorial Building, University of Bristol, Queen's Road, Bristol  
16 BS7 1RJ, UK

17 <sup>7</sup>Isotope Geosciences Unit, SUERC, Scottish Enterprise Technology Park, East Kilbride, G75 0QF, UK

18 \*Now at: Department of Earth Sciences, Durham University, Science Labs, Durham, DH1 3LE, UK

19 Contact: richard.brown3@durham.ac.uk  
20

21 **Abstract**

22 The Igwisi Hills volcanoes (IHV), Tanzania, are unique and important in preserving extra-crater lavas  
23 and pyroclastic edifices. They provide critical insights into the eruptive behaviour of kimberlite  
24 magmas that are not available at other known kimberlite volcanoes. Cosmogenic <sup>3</sup>He dating of olivine  
25 crystals from IHV lavas and palaeomagnetic analyses indicates that they are Upper Pleistocene to  
26 Holocene in age. This makes them the youngest known kimberlite bodies on Earth by >30 Myr and  
27 may indicate a new phase of kimberlite volcanism on the Tanzania craton. Geological mapping, GPS  
28 surveying and field investigations reveal that each volcano comprises partially eroded pyroclastic  
29 edifices, craters and lavas. The volcanoes stand <40 m above the surrounding ground and are  
30 comparable in size to small monogenetic basaltic volcanoes. Pyroclastic cones consist of diffusely  
31 layered pyroclastic fall deposits comprising scoriaceous, pelletal and dense juvenile pyroclasts.  
32 Pyroclasts are similar to those documented in many ancient kimberlite pipes, indicating overlap in  
33 magma fragmentation dynamics between the Igwisi eruptions and other kimberlite eruptions.  
34 Characteristics of the pyroclastic cone deposits, including an absence of ballistic clasts and dominantly  
35 poorly vesicular scoria lapillistones and lapilli tuffs indicate relatively weak explosive activity. Lava  
36 flow features indicate unexpectedly high viscosities (estimated at >10<sup>2</sup> to 10<sup>6</sup> Pa s) for kimberlite,  
37 attributed to degassing and in-vent cooling. Each volcano is inferred to be the result of a small-volume,  
38 short-lived (days to weeks) monogenetic eruption. The eruptive processes of each Igwisi volcano were  
39 broadly similar and developed through three phases: (1) fallout of lithic-bearing pyroclastic rocks  
40 during explosive excavation of craters and conduits (2) fallout of juvenile lapilli from unsteady  
41 eruption columns and the construction of pyroclastic edifices around the vent; and (3) effusion of  
42 degassed viscous magma as lava flows. These processes are similar to those observed for other small-  
43 volume monogenetic eruptions (e.g., of basaltic magma).  
44

45 **Keywords:** kimberlite; Igwisi Hills; explosive eruption; lava; monogenetic volcano  
46

47 **Introduction**

48 Eruptions of ultrabasic kimberlite magmas have never been witnessed, and the dynamics of the  
49 magma's ascent, degassing or dispersal as pyroclasts and lavas at the surface are not well understood.  
50 They are characterised by very low silica contents, high volatile contents and inferred low magmatic  
51 viscosities (Mitchell 1986; Sparks et al. 2006). They originate from great depths (>100 km) and entrain  
52 host rock from the mantle during ascent. There are over 5000 known kimberlite occurrences dating  
53 back to the Early Proterozoic (Kjarsgaard 2007). Due to their great age (>30 Ma) most kimberlites have  
54 had their surface rocks removed by erosion. All that remains for study in most cases are the  
55 volcanoclastic rocks and intrusions preserved within their subterranean volcanic vents (kimberlite  
56 pipes). These rocks are prone to alteration, and primary deposit characteristics are commonly obscured  
57 (e.g., Sparks et al. 2006; Cas et al. 2008; Stripp et al. 2008; Buse et al. 2010). Volcanoclastic rocks  
58 preserved within kimberlite vents have proved problematic to interpret and a number of different, but  
59 not mutually exclusive, processes have been proposed and elaborated for various pipes. These include  
60 fluidisation (Dawson 1971; Field and Scott Smith 1999; Sparks et al 2006; Walters et al. 2006; Gernon  
61 et al. 2008a and b), phreatomagmatism (Lorenz 1975; Ross and White 2006; Lorenz and Kurszlaukis  
62 2007; Kurszlaukis and Lorenz 2008), eruption column collapse (Porritt et al. 2008) and re-  
63 sedimentation (Moss et al. 2008).

64 The Igwisi Hills kimberlite volcanoes (IHV; Sampson 1953; Reid et al. 1975; Dawson 1994)  
65 are thought to be very young (Quaternary) but no reliable radiometric dates have yet been published.  
66 The next youngest kimberlite rocks are Eocene-Oligocene in age (the Kundelungu plateau pipes,  
67 Democratic Republic of Congo, Batumike et al. 2009). Because of their youth, the IHV still preserve  
68 surface rocks and volcanic constructs at the Earth's surface. Kimberlite volcanic rocks emplaced on the  
69 Earth's surface, as opposed to within vents, have great potential to provide insight into eruptive  
70 dynamics, much as they have for other volcanic systems. Examples include bedded and stratified  
71 pyroclastic rocks within ancient kimberlite craters (e.g., Mwadui, Tanzania, Stiefenhofer and  
72 Farrow 2004; Orapa A/K1, Botswana, Field et al. 1997, Gernon et al. 2009a and b, Fontana et al., 2011;  
73 Jwaneng, Botswana, Brown et al. 2008b; Victor pipe, Canada, van Straaten et al., 2011). Extra-crater  
74 examples are rare with the best known being the Fort a la Corne kimberlites, Canada, which have been  
75 intersected by numerous drill cores and interpreted as volcanoes preserving extra-crater rocks  
76 (Berryman et al. 2004; Zonneveld et al. 2004, Kjarsgaard et al. 2007; Pittari et al. 2006). Another  
77 example is the Tokapal kimberlite, India (Mainkar et al. 2004).

78 We present a new geological map for the IHV, and describe and interpret the volcanoes'  
79 morphology, field relationships, lithofacies, macro-scale features and petrography. We present new  
80 geochronological data that confirms a very young (almost Holocene) age for the IHV. We then  
81 compare the IHV to other monogenetic volcanoes and with kimberlite pipes.

82

### 83 **Geological Setting and previous work**

84 The IHV are located on the western side of the Archaean Tanzanian craton, 27kilometres NW of the  
85 village of Urambo (Fig.1). They were emplaced through granitic gneiss basement of the  $2500 \pm 100$  Ma  
86 Dodoman system (see Bell and Dodson 1981). The basement outcrops in small rounded kopjes near  
87 Igwisi village and there are xenoliths in the lavas and pyroclastic rocks. The IHV were first recognised  
88 by the Tanganyikan Geological Survey in the early 1950s (Sampson 1953; Basset 1954; Fozzard 1956;  
89 Dawson 1964). Subsequent studies focused mainly on the petrology of the lava flow from the NE  
90 volcano and its mantle xenoliths (Mitchell 1970; Dawson 1971; Reid et al. 1975; Dawson 1994). Reid  
91 et al. (1975) and Dawson (1994) considered that the Igwisi melts originated at >110 km depth and  
92 concluded that the mineralogy, major element and isotope chemistry of the Igwisi Hills rocks have  
93 strong affinities with calcite-rich kimberlites (e.g. Benfontein sills, South Africa, Dawson and  
94 Hawthorne 1973; see also Mitchell 2008). Mitchell (2008) considered that the IVH magmas depart  
95 from the composition of typical kimberlites due to the presence of hercynitic groundmass spinels that

96 indicate significant crustal contamination. Our geochemical studies (Willcox et al., submitted) of the  
97 IVH support the conclusions of Reid et al. (1975) and Dawson (1994) that they are geochemically  
98 similar to calcitic kimberlites. Little has been published about the physical volcanology of the  
99 volcanoes, except that they are three volcanic centres comprising cones and craters of pyroclastic rocks  
100 and lavas (Sampson 1953; Dawson 1994).

101 The IHV represent the youngest volcanic activity on the Tanzanian craton, which previously  
102 experienced phases of kimberlite volcanism at around 189 Ma (Davis 1977) and 53 Ma (Davis 1977;  
103 Haggerty et al. 1983; Gobba 1989). The IHV are considered the youngest kimberlite volcanoes on  
104 Earth. Dawson (1994) suggested that they are Quaternary in age based on morphological comparisons  
105 with known Quaternary volcanoes in northern Tanzania.

106

## 107 **Methodology**

### 108 *Field study*

109 We undertook detailed geological mapping and sampling of the IHV. Real time kinetic surveying of the  
110 volcanoes was undertaken using a Leica 1200 differential GPS system. Depending on the terrain,  
111 radial, circumferential or orthogonal survey grids with a spacing of <50 m were walked out.  
112 Morphological features, such as ridges, scarps and crater walls, and geological boundaries were  
113 surveyed separately as breaklines. These data were processed in ARCGIS™ to create a DEM that was  
114 then contoured at 2 m intervals (Fig. 2). The DEM was populated with >50 000 xyz points each of  
115 which typically had an accuracy of <1 cm. Several shallow trenches were dug to examine the  
116 subsurface geology away from the volcanoes. We also report the results of petrographic study of the  
117 rocks. Vesicularity, lithic contents and mineral phase abundances were calculated from photographs of  
118 hand specimens and thin sections using ImageJ software (<http://rsbweb.nih.gov/ij/>), and are reported as  
119 volume abundances. The volumes of the volcanic rocks were calculated using 3D models constructed  
120 in Gemcom GEMS™ 3D modeling software from the xyz survey data. We use standard volcanological  
121 and pyroclastic terminology throughout (e.g., Cas and Wright 1987; White and Houghton 2006). Semi-  
122 quantitative grainsize data and sorting parameters for lithofacies were computed in the lab from 1000  
123 length measurements of particles extracted from suitable photographs.

124

### 125 *Cosmogenic <sup>3</sup>He dating*

126 Three samples were taken for cosmogenic He exposure dating. One sample (IH15) was taken from the  
127 eastern summit of the lava coulée of the central volcano under very sparse woodland (Fig. 2). Two  
128 samples (IH52 and IH61) were taken from the NE volcano. Sample IH61 was collected from the  
129 weathered upper parts of the lava flow under sparse woodland (Fig. 2 and 3A). Sample IH52 is from a  
130 scarp cut through the interior of the lava along the eastern crater wall (Fig. 2 and 3B). Samples IH15  
131 and IH61 were considered to be close to the original surface of the lava flows (<1 m). Sample IH52  
132 represents an exposed footwall generated during late-stage subsidence in the NE crater.

133 Olivine was concentrated from the 0.5–1 mm fraction of crushed samples using magnetic and  
134 density techniques. Concentrates were ultrasonically cleaned in 20% HNO<sub>3</sub> and distilled water, and a  
135 pure separate was picked under a binocular microscope. Altered grains and those with adhering basalt  
136 or iron oxide tarnish were removed and the pure separate cleaned in deionized water and then analar  
137 acetone. Magmatic He in trapped gas inclusions was extracted from approximately 1 g of olivine by  
138 crushing in vacuum in an all-metal multi-sample hydraulic crusher. The lattice-hosted He was extracted  
139 from approximately 250 mg of the 100–200 μm grain olivine that remained after crushing. Each sample  
140 was melted during a 20-minute heating period using an 808 nm diode laser (Foeken et al. 2007). In the  
141 case of IH52, two splits were analysed (Table 1). Re-heating after initial melt step yielded no  
142 significant cosmogenic He. Gas clean up procedures and mass spectrometric techniques for helium  
143 isotope ratio determination are reported by Williams et al. (2005). Blank levels for both extraction

144 techniques are governed by the helium background in the mass spectrometer and average  $5 \times 10^3$  and  $5$   
145  $\times 10^8$  atoms of  $^3\text{He}$  and  $^4\text{He}$  respectively. These amounts represent less than 0.1% of the sample helium.  
146 The reproducibility of standard He abundance determinations over the two periods of analyses were 1%  
147 for  $^3\text{He}$  and 0.5% for  $^4\text{He}$ . Analytical uncertainties reported in Table 1 are propagated from uncertainties  
148 in the  $^3\text{He}$  and  $^4\text{He}$  concentrations.

#### 149 *Palaeomagnetic study*

151 To further help constrain the age of the Igwisi Hills lavas, twenty oriented 25mm diameter cores were  
152 collected, using a portable rock drill, from the lava flows for palaeomagnetic analysis. Samples were  
153 oriented in the field with sun and magnetic compasses, and were subsequently cut in the laboratory into  
154 standard cylindrical specimens, with most cores yielding two or more specimens. A total of 29  
155 specimens from 17 samples were subjected to progressive thermal (14 specimens) or alternating field  
156 (AF) (15 specimens) demagnetisation, using a minimum of 14 steps, up to peak temperature of  $580^\circ\text{C}$   
157 or peak AF fields of 100mT. The natural remanent magnetisation (NRM) of the specimens was  
158 measured at each step with a Molspin Spinner magnetometer or a 2G cryogenic magnetometer housed  
159 in a magnetically shielded room at the University of Oxford. Components of magnetisation were  
160 identified using principal component analysis of linear segments in the demagnetisation trajectories,  
161 where lines were defined by a minimum of five consecutive points.

#### 163 **The Igwisi Hills volcanoes (IHV)**

164 The IHV are three small volcanic centres (NE, central and SW volcanoes) comprising pyroclastic  
165 cones, craters and lavas (Fig. 2 and 3C–E). Together they constitute  $>3.2 \times 10^6 \text{ m}^3$  (Table 2) of erupted  
166 products and cover  $>2.7 \times 10^5 \text{ m}^2$ . The relative ages of the IHV cannot be fully constrained, although  
167 field relationships indicate that the central volcano postdates the NE volcano. They are aligned NE–SW  
168 and sit upon a broad, low NE–SW-oriented ridge, 500 m wide and 16 m high that is probably  
169 composed of pyroclastic material (poorly exposed) from early stages of the eruptions. The volcanoes  
170 have been partially buried by younger sediments and soils, and are presently covered in grassland and  
171 low-density forest. They exhibit similar pyroclastic lithofacies, which are summarized in Table 3.  
172 Pyroclastic rocks are lithified with calcite cement, which means that standard granulometric analyses  
173 commonly applied to loose pyroclastic deposits cannot be used. Morphological, structural and  
174 lithological features of each volcano are outlined below. Note that many of the large olivine crystals in  
175 the IHV are multigrain aggregates and can be regarded as micro mantle xenoliths (Dawson 1994).

#### 177 *NE volcano*

178 The NE volcano covers  $>1.9 \times 10^5 \text{ m}^2$  and comprises a flat-bottomed sub-circular crater  $\sim 200 \times 200 \text{ m}$   
179 in diameter surrounded by a partial low ring of outward-dipping pyroclastic rocks and by lava (Fig. 2  
180 and 3C). The crater floor (1088 masl) is at or just below the inferred height of the palaeo-surface.  
181 Crater walls on the northern side of the crater comprise a succession of bedded pyroclastic rocks; the  
182 eastern side comprises lava. The northern and western crater walls are presently 4–8 m higher than the  
183 eastern crater wall (Fig 2 and 3C). The south-western crater wall has been buried by lava from the  
184 central volcano (Fig. 2).

#### 186 *Pyroclastic rocks*

187 The oldest exposed pyroclastic rocks are grey, bedded lithic-bearing coarse tuffs and lapillistones  
188 (blT/blL, see Table 3 and Fig. 4). They are exposed along the inner crater wall on the north of the  
189 volcano and in patchy outcrops on the ground on the northern exterior of the volcano. Similar tuffs  
190 were encountered in a shallow trench dug radially away from the central volcano (trench 1, Fig. 2).  
191 They were not encountered in the other trenches dug to depths of  $>2 \text{ m}$  (Fig. 2). These tuffs reach 8 m

192 thick in the crater wall and we infer that they form a wide apron extending at least several hundred  
193 metres away from the NE and central volcanoes, although their base, and the pre-eruption substrate is  
194 not exposed and the apron is mostly covered by soil. Along the inner crater wall the abundance of lithic  
195 clasts in these pyroclastic rocks varies between 5–40 vol. % with a typical abundance of 5–12 vol.  
196 %. There are two types of pyroclasts in this lithofacies. The first are non-vesicular, crystalline and have  
197 irregular and amoeboid to subspherical shapes and are up to several millimetres in diameter (Fig. 5A).  
198 The second (pelletal clasts) comprise lithic clasts, olivine crystals and olivine micro-xenoliths  
199 surrounded by a thin, uneven coating of solidified kimberlite magma (Fig. 5A).

200 Overlying the lithic-bearing lithofacies on the north and north-east side of the NE volcano are  
201 juvenile clast-rich pyroclastic deposits. These comprise bedded juvenile-rich tuffs and lapillistones  
202 (bT/bL), and pelletal clast-rich tuffs and lapillistones (bpelT/bpelL, Table 3; e.g., Fig. 6). Together they  
203 exceed 10 m in thickness and are inferred to have originally formed a partial cone with a preserved  
204 volume of  $3.1 \times 10^5 \text{ m}^3$ . No pattern was recognised in the alternation of the two lithofacies. Individual  
205 beds are typically 3–30 cm thick and are not traceable between outcrops (i.e. over metres to 10s-of-  
206 metre scale) due to an absence of marker horizons and poor outcrop quality. Bedding is defined by  
207 changes in grain size or by alternations between the two lithofacies. Normal-graded, reverse-graded and  
208 non-graded beds are present. Beds dip outwards from the crater at angles of 16–28° with an average dip  
209 of 21° (Fig. 2). In the south-east of the volcano ~4 m of poorly exposed tuff and lapillistone outcrop  
210 between the NE volcano lava and the central volcano (Fig. 2). Similar rocks are poorly exposed beneath  
211 lavas in the NE crater wall (Fig. 2).

212 Three types of pyroclasts occur within these juvenile-rich pyroclastic deposits. The first type is  
213 incipiently vesicular scoria clasts up to coarse lapilli size with irregular, angular shapes (e.g., Fig. 5B  
214 and C). The edges of the scoria clasts cut through vesicles and there is no evidence for vesicle zoning  
215 or chilled exteriors. These have 10–20 vol. % subspherical, elongate to irregular-shaped vesicles, 0.02–  
216 3 mm in diameter, some of which show evidence for coalescence (Fig. 5C). Vesicles have been  
217 partially filled with secondary calcite. The second are pelletal lapilli comprising olivine crystals and  
218 micro-xenoliths which reach 10 mm in diameter. They are coated in a thin jacket of crystalline  
219 kimberlite groundmass, which is typically a few 10s of  $\mu\text{m}$  thick (Fig. 5D), but in many cases only  
220 partially encloses the central grain. The third type are olivine aphyric sub-spherical, rounded dense  
221 juvenile lapilli <3 cm in diameter. These latter pyroclasts are rare, accounting for <2–5 % of the  
222 pyroclast populations.

### 224 *Lava*

225 The eastern sector of the NE volcano comprises predominantly kimberlite lava (Fig. 2 and 3C). The  
226 mineralogy and petrology of the lava have been described and discussed in detail by both Reid et al  
227 (1975) and Dawson (1994), and here we concentrate on physical features. The lava's original upper  
228 surface is not preserved, but it overlies poorly exposed lithic-rich tuffs and is at least 2.6 m thick. It is  
229 generally poorly exposed along the eastern inner crater wall, and is mostly buried under soil and  
230 younger sediments away from the volcano (Fig. 2). The best section through the lava is in the NE  
231 sector of the volcano to the east of a prominent notch in the crater walls (Fig. 2). It has a fine-grained  
232 crystal-poor base and an olivine crystal- and micro-xenolith-rich lower third (Fig. 7). Imbricated  
233 olivine crystals and xenoliths within the lava indicate flow towards the SSW, i.e. back into the crater.  
234 Large olivine crystals and micro-xenoliths vary in abundance through the lava, but generally decrease  
235 in abundance upwards (from 26 vol. % to 5 vol. %), above the thin olivine-poor base (Fig. 6). The  
236 upper parts of the lava are poorly vesicular (<15 vol. %). Vesicles vary from 1–40 mm in diameter, are  
237 sub-spherical to irregular in shape and some are sheared and coalesced (Fig. 7). Most vesicles are lined  
238 with a thin coating of carbonate.

239 The lava forms a broad irregular eroded plateau-like feature, ~200 m long by 100 m wide, on  
240 the eastern side of the volcano and exhibits metre-scale topography (Fig. 2 and 3C). The plateau rises  
241 up to 16 m above the crater floor (Fig. 2) and exhibits a crudely-defined, stepped morphology down  
242 into the crater over a distance of <50 m. The plateau passes into a flat-lying poorly exposed lava flow  
243 that extends northeast for >500 m. The lobate margin of the latter lava flow (Fig. 2) has been defined  
244 by scattered outcrops and by the location of loose lava blocks and boulders on the forest floor. The lava  
245 forming the eastern plateau overlies a thin wedge of outward-dipping pyroclastic rocks exposed  
246 beneath the lava in the NE and SE crater wall (Fig. 2). In total, lava from the NE volcano covers  $>1.5 \times 10^5$  km<sup>2</sup>  
247 (including lava in the crater) and assuming an average thickness of 2.5 m it has a minimum  
248 volume of  $>3.7 \times 10^5$  m<sup>3</sup>. The flat-lying lava flow covers  $8 \times 10^4$  m<sup>2</sup> and, assuming a similar average  
249 thickness, has a volume of  $\sim 2 \times 10^5$  m<sup>3</sup>. Lava is not exposed on the northern or western walls of the  
250 crater, but is inferred to underlie the gently inward-dipping margins of the crater along the north and  
251 west sides of the crater (Fig. 2).

252

### 253 **Central volcano**

#### 254 *Morphology and physical structure*

255 The central volcano covers  $>8.1 \times 10^4$  m<sup>2</sup> and has a minimum basal diameter of >300 m. It is  
256 surrounded to the west and north-west by an eroded apron of lithic-bearing coarse tuff (Fig. 2). The  
257 western side comprises a N–S oriented elongate partial cone of outward-dipping bedded pyroclastic  
258 rocks, in which beds dip towards the W, NW and SW (Fig. 2 and 3D). This pyroclastic mound rises 36  
259 m above the surrounding plain and has outer slopes of  $\sim 24^\circ$ . The eastern margin of the mound is an N–  
260 S oriented, near-vertical crater wall. The crater currently sits beneath a thick lava flow (Fig. 2 and 3D).

261

#### 262 *Pyroclastic rocks*

263 The pyroclastic cone has a minimum volume of  $1.4 \times 10^5$  m<sup>3</sup> and comprises bedded juvenile-rich  
264 lapillistone, lapilli-tuffs and tuffs (bT/bL and bpelT/bpelL, Fig. 6A–F, Table 3) that are texturally  
265 similar to those of the NE volcano. Juvenile clasts reach 7 cm in diameter but most are <1.5 cm in  
266 diameter. Rare lithic clasts never exceed 10 cm in diameter (Fig. 6F). Tracing individual beds laterally  
267 is difficult due to discontinuous outcrops. Thin coarse tuff beds are intercalated with the coarse-grained  
268 lapilli-tuff and lapillistone beds and reach several centimetres in thickness. Clasts in these beds have  
269 been cemented together with calcite that is absent in the outer 2–3 cm thick weathered rind of most  
270 outcrops. Pyroclasts are similar to those found in the pyroclastic deposits of the NE volcano and are  
271 described above and in Table 2. Beds in the pyroclastic cone dip outwards at 15–32° (Fig. 2) with an  
272 average dip of 21°.

273

#### 274 *Lava*

275 The crater of the central volcano is filled with a lava flow, which was previously mapped as pyroclastic  
276 rocks (see Sampson 1953). It is 150 × 300 m in diameter, is >25 m thick and covers a minimum area of  
277  $>3.4 \times 10^4$  m<sup>2</sup> (Fig. 2 and 3D). It has a minimum volume of  $4 \times 10^5$  m<sup>3</sup> (calculated above inferred  
278 palaeo-surface). The overall morphology is of a asymmetric mound with two bounding levees either  
279 side of a slightly lower central channel open to the southeast. Its western margin abuts against the crater  
280 wall of the pyroclastic cone (Fig. 2 and 3D). The northern and eastern slopes of the lava are steep (29–  
281 32°) and are partially covered by soil and talus rocks, while the south-west slope is much shallower (2–  
282 3°). Its southwest margin is inferred from the position of large blocks of lava and scattered outcrops on  
283 the forest floor that define a broad, lobate terminus 180 m wide (Fig. 2).

284 The lava is dense, homogeneous, reddish-brown, and contains scattered basement inclusions  
285 (Fig. 8A and B). Rounded olivine xenocrysts >5 mm account for >2 vol. % of the rock. It has a fine- to  
286 medium-grained serpentine-calcite-apatite-spinel-perovskite groundmass. Basement clasts are

287 commonly recess-weathered and range in diameter from <0.1–8 cm in diameter (Fig. 8A). They are  
288 typically rounded and are granitic or dioritic in composition. Unaltered biotite is a prominent  
289 constituent of many of the basement inclusions. They are irregularly scattered throughout the lava and  
290 reach 2.5–5.5 vol. %. Parallel, curving and cross-cutting centimetre-spaced joint sets are present within  
291 the rock.

292

### 293 ***SW volcano***

294 The SW volcano is located 500 m southwest of the central volcano (centre-to-centre, Fig. 2 and 3E). It  
295 comprises a sub-circular pyroclastic cone that covers  $>8.1 \times 10^5 \text{ m}^2$ , has a basal diameter of  $>300 \text{ m}$ ,  
296 and rises over 30 m above the surrounding ground (Fig. 2 and 3E). The north and west walls of the  
297 crater are 14 m higher than the south and east side and are breached to the northeast. The slopes of the  
298 cone dip  $\sim 17^\circ$  on the west and north and  $15^\circ$  on the east and south (Fig 2). It has a  $180 \times 140 \text{ m}$  flat-  
299 bottomed crater perched 12 m above the surrounding ground (Fig. 2).

300

### 301 ***Pyroclastic rocks***

302 The pyroclastic cone of the SW volcano has a minimum volume of  $9 \times 10^5 \text{ m}^3$ . The oldest pyroclastic  
303 rocks are massive lithic-bearing tuffs (bT/bL, Table 3), exposed in a 50 m-wide notch on the northern  
304 side of the cone (Fig. 3E). They reach several metres thick and also crop out in the surrounding plain  
305 up to several 10s metres away from the volcano (Fig. 2). They are compositionally similar to lithic-rich  
306 tuffs at the other two volcanoes and look similar in thin-section. They are overlain by 8 metres of  
307 massive to bedded juvenile clast-rich lapillistone (mbL, Table 3), which outcrops along the western  
308 inner crater wall. This passes upwards into bedded juvenile-rich tuff and lapillistone (bt/bL and  
309 bpeLT/bpeLL, Table 3). Bedding planes dip outwards at  $6\text{--}31^\circ$  (Fig. 1) and bedding is steeper on the  
310 eastern side of the volcano ( $<31^\circ$ ) than on the west ( $<24^\circ$ ; Fig. 2).

311

### 312 ***Lava***

313 A short, poorly exposed lava crops out at the base of the eastern flank of the SW volcano. Its extent has  
314 been estimated by scattered outcrops and by the position of loose lava blocks on the forest floor (Fig.  
315 2). It covers  $>4000 \text{ m}^2$  and is mostly buried by soil. It is texturally similar to the lava from the NE  
316 volcano, is poorly vesicular and contains 5–8 % rounded olivine crystals and olivine micro-xenoliths.  
317 Vesicles reach 1 cm in diameter, are highly irregular in shape and account for  $<12 \text{ vol. \%}$  of the rock.  
318 The base of the lava is not seen and its upper surface is not preserved. It exhibits features similar to  
319 shallow levees that run up the eastern side of the pyroclastic cone towards a 30 m wide shallow notch  
320 in the crater wall (Fig. 2). It appears to have flowed out of the crater and may indicate that the perched,  
321 flat-bottomed crater of the SW volcano is the solidified crust of a lava lake.

322

### 323 **Groundmass mineralogy**

324 Petrological aspects and mineral chemistry of the NE lava are described in detail by Reid et al. (1975),  
325 Dawson (1994) and Buisman et al. (submitted). Here we outline the key mineralogical features of the  
326 Igwisi volcanic products.

327

### 328 ***Lavas***

329 The dominant mineral phase in the NE lava is olivine, which occurs as spheroidal to ellipsoidal  
330 xenocrysts, smaller irregular shaped phenocrysts and as inclusions in titanomagnetite (Fig. 9A, B and C  
331 respectively). Olivine crystals exhibit minimal alteration (serpentinisation) and are set in a fine- to  
332 medium-grained serpentine-calcite-spinel-apatite-perovskite groundmass (Fig. 10B, C and D).  
333 Phlogopite crystals are rare in all samples. Most phlogopite grains are euhedral K-phlogopite with Ba-  
334 rich (kinoshitalite) overgrowths (Fig. 9D) with a few either pure kinoshitalite or phlogopite.

335 Monticellite is present in some samples (Fig. 9E). The spinels are mainly titanomagnetite with thin Mg-  
336 Al-spinel rims: a few have Mg-Al-chromite cores (e.g. Fig 9F). Cr-spinel is found as small euhedral  
337 inclusions in the olivine xenocrysts.

338 The NE lava flow exhibits subtle variations: lower parts contain tabular calcite as laths and  
339 crystalline grains (Fig. 10D). Some olivine xenocrysts are mantled by perovskite and Mg-Al-spinel at  
340 the grain's greatest curvature: this coating thins towards the equator of the grain (Fig. 9A; see Dawson  
341 1994). Groundmass minerals include apatite hopper crystals, perovskite and monticellite. The upper  
342 parts of the NE lava show a higher degree of alteration (Fig. 10C). Apatite hopper crystals are filled  
343 with serpentine and fine-grained amorphous aggregates of hydrogarnet. Calcite is mostly found as  
344 spongy, tabular laths but occasionally as crystalline amorphous aggregates. Most spinels show partial  
345 replacement of Mg-Al-spinel rims by hydrogarnet, but some are completely replaced and occur as  
346 spinel pseudomorphs consisting of serpentine rims enclosing hydrogarnet (Fig 9G). Serpentine  
347 replacing olivine and in the groundmass has an unusual Al-rich composition and has been recognised  
348 as a new variety consisting of interlayers of end member serpentine and hydrotalcite (Willcox et al.,  
349 submitted).

350 The mineralogy of the central (Fig. 10B) and SW volcanoes' lavas is closely similar to that of  
351 the NE lava flow. The rims of olivine xenocrysts are partially resorbed and some smaller forsteritic  
352 xenocrysts are pseudomorphed by serpentine, brucite and calcite. The groundmass is mostly serpentine  
353 and calcite with small amorphous grains of apatite, hydrogarnet and perovskite. The SW and central  
354 volcano lavas exhibit greater abundances of hydrogarnet in the groundmass: some spinel rims (Mg-Al-  
355 spinel) have been partially to completely replaced by hydrogarnet. All lavas contain variable  
356 proportions of secondary minerals such as serpentine, barite, witherite, and hydrogarnet.

#### 357 358 *Pyroclastic rocks*

359 The pyroclastic rocks contain large rounded olivine xenocrysts (8–18 vol. %; Fig. 10A), which show  
360 large proportions of resorbed rims. The groundmass in juvenile pyroclasts is serpentine-poor (in  
361 comparison to the lavas) and contains larger apatite, perovskite and hydrogarnet grains (Fig. 9H).  
362 Serpentine is mostly found replacing forsterite inclusions in titanomagnetite and in partial to complete  
363 replacement of olivine xenocrysts (pseudomorphs). Spinel grains are rare and some contain forsterite  
364 inclusions. The rims of most spinels have been partially replaced by hydrogarnet. The pore space in the  
365 rocks is filled predominantly by calcite (Fig. 10A and 9H) and minor dolomite (Fig. 9H).

#### 366 367 **Cosmogenic <sup>3</sup>He dating results**

368 Helium concentrations and isotopic compositions are presented in Table 1. Exposure ages of all  
369 samples are calculated using the equations in Kurz et al. (1987) and assumes no correction is required  
370 for implanted or *in situ* radiogenic <sup>4</sup>He. A sea level high latitude production rate of  $120 \pm 9$  atoms/g/year  
371 (Goehring et al. 2010) was scaled for altitude and latitude using factors of Dunai (2000). Sparse  
372 vegetation cover (trees and bushes) is present at all samples sites but has not been sufficient to require  
373 correction, and no depth correction or self-shielding corrections were necessary. Topographic shielding  
374 is significant (~30%) for sample IH52. Exposure ages range from 5.9–12.4ka (Table 1). The low  
375 concentration of cosmogenic <sup>3</sup>He has resulted in relatively large age uncertainties, in one case up to 70  
376 %. The arithmetic mean of the exposure ages suggest that the Igwisi Hills volcanoes were erupted at  
377  $8.9 \pm 2.7$  ka ( $1\sigma$ ,  $n = 4$ ). However, IH15 and IH61 have probably experienced a small degree of  
378 erosion, which suggests that the slightly older ages determined for sample IH52 ( $11.2 \pm 7.8$  and  $12.4 \pm$   
379  $4.8$ ka) are better estimates of the eruption age.

#### 380 381 **Palaeomagnetic results**

382 All of the 29 specimens from the 17 samples subjected to palaeomagnetic analysis yielded well-defined  
383 components of magnetisation. After removal of a randomly oriented component of magnetisation by Af  
384 fields of 12mT or temperatures of 200°C a stable characteristic remanence was isolated in all  
385 specimens. We attribute the low-stability component to a viscous magnetisation acquired post-  
386 sampling. The characteristic remanence was well grouped in 22 specimens from 12 samples, yielding a  
387 mean declination of 357.6° and a mean inclination of 6.1° ( $k=23.9$ ;  $\alpha=9.1^\circ$ ; Fig. 10). The 7 specimens  
388 that yield stable magnetisations with anomalous directions were characterised by abnormally high  
389 NRM intensities, and we suspect that those outcrops had been subjected to lightning strikes. The mean  
390 direction obtained from the bulk of the lava samples is very close to the expected present field direction  
391 of the Igwisi Hills (Fig. 11), and is consistent with a young age for the lava, both in term of the  
392 direction and polarity of the lava.

### 394 **Post-emplacement changes to Igwisi Hills**

395 The IHV are young landforms that have undergone weathering, alteration, cementation and erosion  
396 since emplacement. The pyroclastic rocks are cemented by calcite and exhibit an unusual weathering  
397 style interpreted as dissolution (carbonation) features similar to grikes in Karst landscapes (Dawson  
398 1994). There is little evidence that material weathered from the volcanoes has been transported away  
399 by surface water and less-soluble components (olivine crystals, lithic clasts) weathered from the tuffs  
400 have accumulated on the flanks of the volcanoes. Studies of modern volcanic craters indicate that their  
401 rims recede rapidly following eruption and feed scree slopes along the crater wall base, before  
402 stabilising (e.g., Pirrung et al. 2008; see also White and Ross 2011). Crater walls of the 1977 Ukinrek  
403 maars receded by 20 m over 27 years (Pirrung et al. 2008). Scree slopes are generally absent along the  
404 interior crater wall for the NE volcano (Fig. 2) and we suggest that the NE volcano's crater rims have  
405 receded little (metres) since emplacement.

### 407 **Discussion**

#### 408 ***Emplacement of pyroclastic rocks***

409 Two phases of pyroclastic activity are recorded at each of the IHV (Fig. 12). The pyroclastic rocks that  
410 make up the tephra cones of the IHV share some broad characteristics including centimetre to  
411 decimetre-scale bedding defined by sharp to gradational variations in the abundances and grainsizes of  
412 lithic clasts, olivine crystals or juvenile clasts (Table 3, Fig. 4; Fig. 5E); well to very well sorted ( $\sigma_\phi =$   
413  $0.75-2$ ; following Cas and Wright, 1987), a framework-supported texture of coarse ash and lapilli-sized  
414 clasts and a general absence of fine ash ( $< 200\mu\text{m}$ ; Fig. 5A–C). The lateral extent of many beds is not  
415 known due to poor exposure, but the absence of recognizable tractional structures (e.g., dune bedforms)  
416 or erosion features suggests that they are fall deposits. Although this cannot be proven in all cases,  
417 most beds are persistent across individual outcrops (metre-scale). The rapid vertical changes in  
418 grainsize, composition and abundance of coarse fragments over centimetres to decimetres suggest  
419 deposition from numerous small explosions. We infer that the pyroclastic accumulated from unsteady  
420 eruption plumes that resulted from numerous closely-spaced discrete explosions. Steady conditions are  
421 recorded by thick massive beds in the SW volcano (lithofacies mbL, Table 3).

422 Contacts between the pre-eruption substrate and oldest pyroclastic rocks at each volcano are not  
423 exposed and neither are deposits from the opening phases of the eruptions. The oldest exposed  
424 pyroclastic rocks at each volcano are enriched in lithic clasts (lithofacies blT/blL; Fig.4 and 5A, Table  
425 3), suggesting that early phases involved a degree of vent erosion. The overlying pyroclastic deposits,  
426 which contain virtually no lithic clasts and which make up the bulk of the tephra cones, are inferred to  
427 record eruptions with little or no vent erosion.

428 The pyroclastic edifices of all three volcanoes are built higher on their west and northwest sides  
429 (Fig. 2). This is most marked in the central volcano and is consistent with fallout from small, weak

430 eruption plumes(1–4 km) that were sheared by the dominant south-easterly trade winds ( $\sim 13 \text{ ms}^{-1}$ ).  
431 Asymmetry due to wind shearing of plumes is common in small pyroclastic cones (e.g., Porter 1972).  
432 Similar interpretations have been proposed to account for volcano asymmetry identical to that of the  
433 IHV shown by some young maars and tuff cones in northern Tanzania (Dawson and Powell 1969;  
434 Mattsson and Tripoli 2011).

### 435 436 *Emplacement of lavas*

437 All three IHV record late-stage effusion of small volumes of degassed kimberlite magma (Phase 3, Fig.  
438 12) that fed dense to poorly vesicular ( $<15 \text{ vol. } \%$ ) lavas that travelled short distances from their vents  
439 (Fig. 2). Walker (1973) demonstrated a correlation between lava effusion rate and lava length over a  
440 wide range of lava viscosities and substrate slope angles. Using Walker's empirical relationships as a  
441 guide, we can constrain the effusion rates of the IHV lavas to  $<1 \text{ m}^3/\text{s}$ , which gives emplacement times  
442 of up to 2 days. The thicknesses and physical features of the IHV lavas suggest relatively high effective  
443 viscosities.

444 Kimberlite magmas with silica contents of  $<25 \text{ wt } \%$  (e.g., Mitchell 1986) are inferred to have  
445 low melt viscosities ( $0.1\text{--}1 \text{ Pa s}$ , Sparks et al. 2006). Large olivine crystals are concentrated in the lower  
446 third of the NE lava flow, but do not appear to form a cumulate layer (the crystals are not touching, Fig.  
447 7). This observation can be used to place a first-order lower limit on the viscosity of the lava by using  
448 Stoke's Law (e.g., Rowland and Walker 1988). The concentration of olivine crystals towards the base  
449 of the lava (Fig. 7) could be interpreted as due to syn- and post-emplacement settling of crystals or the  
450 consequence of co-eruption of crystal-rich and crystal-poor with denser crystal-rich lava being  
451 emplaced at the base of the flow. We favour the latter explanation. The olivine crystals are not touching  
452 (Fig. 7) as would be expected if they had settled from an original uniform distribution and aggraded at  
453 the base. They also show imbrication, indicative of in situ orientation in a shear flow. The lack of  
454 settling within the basal crystal-rich 50 cm zone can be used to estimate a lower bound on viscosity. A  
455 time scale,  $t$ , can be constrained by the usual conductive scaling law in which  $t \sim l^2/k$ , where  $l$  is a  
456 characteristic length and  $k$  is the thermal diffusivity. Taking  $l = 0.25 \text{ m}$  and a typical value of  $k = 6 \times$   
457  $10^{-7} \text{ m}^2/\text{s}$ , a time scale of 28 hours (about 1 day) is calculated. Using Stokes law, a crystal diameter of 5  
458 mm and a density contrast between olivine and surrounding melt of  $500 \text{ kg/m}^3$ , the viscosity for an  
459 olivine to sink 0.25 m in this time is approximately  $2700 \text{ Pa s}$ . This is not an exact threshold but if the  
460 viscosity had been much lower than this value then some settling and touching of olivine crystals might  
461 have been expected. Another explanation of the lack of settling is that the groundmass was partially  
462 crystallized or crystallising during emplacement, and evidence for this is provided by the flow-aligned  
463 groundmass calcite crystals. A partially crystallized groundmass can increase lava viscosity and also  
464 result in development of a yield strength (Castrucchio et al., 2010). From these considerations we infer  
465 that the lava has a viscosity likely around or above  $10^3 \text{ Pa s}$ . Additionally the nature of the residual  
466 melts during emplacement is not well constrained due to formation of abundant serpentine replacing  
467 unknown phases (Willcox et al., submitted).

468 The lava covering the eastern plateau of the NE volcano (Fig. 2) is inferred to overlie low-lying  
469 parts of the outward-dipping pyroclastic cone. The presence of lava  $>10 \text{ m}$  above the crater floor  
470 suggests that the either crater must at some stage have been filled with lava up to this level, or that  
471 high-high-standing lava is clastogenic in origin, although we found no positive evidence for this (e.g.,  
472 draping of crater walls or remnant pyroclastic textures in the lava). We interpret the lava on the eastern  
473 plateau to have been fed by overflows from a late-stage perched lava lake that filled the crater. We  
474 infer from flow directions given by olivine imbrication that this lava drained back into the crater. The  
475 present bowl-shaped crater is interpreted to have formed by subsidence of this lava lake. Withdrawal  
476 may have been caused by magma becoming diverted to a neighbouring volcano, by breaching of the  
477 pyroclastic cone around the NE volcano crater, or by some combination of both. Additionally,

478 compaction of the vent-filling pyroclastic material may have contributed to the subsidence of the crater  
479 floor (e.g., Lorenz 2007). Lava drain out through a cone breach is strengthened by the comparable  
480 volume estimates of the empty crater ( $1.9 \times 10^5 \text{ m}^3$ ) and the flat-lying lava flow to the northeast ( $2 \times$   
481  $10^5 \text{ m}^3$ ), and by the presence of a prominent notch in the north crater walls (Fig. 2). We thus infer that  
482 the lava breached the pyroclastic cone in the NE of the crater and spread out across the ground. We  
483 interpret the stepped morphology along the inner eastern crater wall as the result of a series of partial  
484 circumferential faults, downthrown towards the crater, that were generated by subsidence following  
485 draining of the lava lake (Fig. 2). Lava does not outcrop along the northern and western walls of the  
486 crater, but we infer the tilted surface of this subsided lava lake underlies the shallow, inward-dipping  
487 slope in these parts (Fig. 2).

488 The lava of the central volcano is interpreted as a viscous lava coulée (Fig. 2). The presence of  
489 altered crustal inclusions (2.5–5.5 vol. %) dispersed through the lava is puzzling (Fig. 8). Mixing cold  
490 lithic clasts into lava is difficult. Similar lithic-bearing, igneous-textured layered rocks within other  
491 kimberlite pipes, in some cases at depths of  $>1 \text{ km}$  have been interpreted as welded pyroclastic rocks  
492 that result from the mixing of fragmented lithic material and hot juvenile clasts within an explosive  
493 pyroclastic jet or fountain (e.g., Sparks et al. 2006; Brown et al. 2008a, 2009; van Straaten et al., 2011).  
494 Texturally similar rocks in basaltic volcanic systems have also been interpreted as welded pyroclastic  
495 rocks from weak inefficient fountains (McClintock et al., 2008). The morphology of the central  
496 volcano lava coulée seems incompatible with in-situ deposition from a fountain as there is no evidence  
497 for layering within the lava or for mantling of the adjacent cone by welded pyroclastic deposits. Either  
498 the lithic clasts were incorporated at depth, when the magma was at a low viscosity, or the coulée  
499 represents a densely welded pyroclastic rock that accumulated in the conduit and was subsequently  
500 extruded as a viscous plug. Biotite is stable in the altered basement xenoliths within the central volcano  
501 coulée and this constrains its emplacement temperature to below about  $850^\circ\text{C}$  (Douce and Beard 1994).  
502 The consistent palaeomagnetic directions indicate emplacement temperatures above the Curie  
503 temperature for groundmass titanomagnetite ( $550^\circ\text{C}$ ).

504

### 505 **Comparison with other small monogenetic volcanoes**

506 The IHV are small volcanoes with minimum volumes of preserved surface volcanic products of  $\sim 10^6$   
507  $\text{m}^3$  (Table 2). The volumes of erupted material dispersed away from the volcanoes by ash clouds during  
508 the eruptions and removed from the volcanoes by erosion are not known, but accounting for this would  
509 mean that the IHV eruptions were probably at least VEI 2 in magnitude ( $>0.01 \text{ km}^3$ , e.g., Newhall and  
510 Self 1982). This is typical for small monogenetic eruptions.

511 The well preserved nature of the IHV allows comparison with other types of monogenetic  
512 volcanoes (scoria cones, tuff rings, tuff cones and maars, see Wood 1980; Wohletz and Sheridan 1983;  
513 White and Ross 2011). The IVH have been eroded and comparisons based on edifice morphology need  
514 to be made with caution. Bedding dips in pyroclastic edifices of the IHV vary from  $4\text{--}32^\circ$  with mean  
515 dips of  $18\text{--}21^\circ$  (Fig. 2). These dips are lower than those typical of scoria cones (critical angle of repose,  
516  $30\text{--}35^\circ$ ), but are similar to those of small phreatomagmatic volcanoes (e.g., tuff rings, tuff cones and  
517 maars, White and Ross, 2011). The NE volcano resembles a small maar volcano or tuff ring with its  
518  $\sim 200 \text{ m}$ -wide crater sitting at or just below the palaeo-surface. It is small for a maar volcano, which  
519 have mean diameters in the range  $340\text{--}550 \text{ m}$  (Ross et al. 2011). The pyroclastic edifice of the central  
520 volcano is partly buried by later-erupted lava, but in terms of bedding dips, it compares to tuff cones.  
521 The SW volcano has a well-developed cone morphology, dip angles mostly below the angle of repose  
522 and a perched crater, and morphologically resembles a tuff cone or scoria cone.

523 Tuff cones and maar volcanoes commonly show textural and physical evidence in both deposits  
524 and pyroclasts for explosive interaction with ground or surface water. This can lead to a suite of  
525 features that may include elevated quantities of lithic clasts in pyroclastic deposits (e.g., Fisher and

526 Schmincke 1984; Valentine 2012), large ballistic lithic clasts, crudely bedded and stratified pyroclastic  
527 deposits, dense to poorly vesicular pyroclasts (e.g., Wohletz and Sheridan 1983), fine ash layers and ash  
528 aggregates (e.g., accretionary lapilli), and edifices comprised of both pyroclastic density current  
529 deposits (less common in tuff cones) and pyroclastic fall deposits (see White and Ross 2011; Valentine,  
530 2012). The IHV exhibit lithic-bearing crudely bedded pyroclastic deposits (lithofacies bIT and bIL,  
531 Table 3) and dense or poorly vesicular pyroclasts (Phase 1, Fig. 4 and 5A). Fine ash layers, ash  
532 aggregates and pyroclastic density current deposits were not observed (note: ash aggregates and  
533 pyroclastic density current deposits have been found in other kimberlite pipes, e.g., Venetia pipes,  
534 Kurszlaukis and Barnett 2003; Jwaneng pipes, Brown et al. 2008b; Orapa pipes, Gernon et al. 2009a;  
535 Porritt and Russell in press). Large ballistic lithic clasts are absent in the IHV even in ultra-proximal  
536 deposits. Clasts >5 cm in diameter are rare and clasts >10 cm in diameter are extremely rare at each  
537 IHV (e.g., Fig. 6F). Large juvenile bombs (>50 cm in diameter) also common in proximal settings  
538 during monogenetic eruptions are similarly absent in the IHV. The small juvenile pyroclast size (coarse  
539 ash to fine lapilli) probably reflects the explosive disruption of predominantly low viscosity magma:  
540 this is backed-up by the droplet shapes of many kimberlite pyroclasts (e.g., Mitchell 1986; Moss et al.  
541 2011). The absence of large lithic ballistic clasts is puzzling, because even weak explosions eject  
542 coarse lithic clasts over proximal areas. One possibility is that explosions were occurring at depth in the  
543 conduits, and large clasts could not escape (e.g., Sparks et al. 2006). This remains to be explored as a  
544 possibility at the IHV. There is little preserved environmental evidence for surface water at the time of  
545 the IHV eruptions but it is possible that ephemeral surface water was present. The country rock  
546 comprises crystalline basement—potentially a poor aquifer for driving maar eruptions.

547 The IHV pyroclastic edifices share similarities with small cones formed by basaltic magmatic  
548 eruptions. The Phase 2 juvenile-rich pyroclastic deposits (e.g., lithofacies bL, bpell, Table 3) contain  
549 very low volumes of lithic material, comparable to the volumes common in basaltic scoria cones (e.g.,  
550 Valentine and Groves 2008; Valentine 2012). The crude bedding and stratification of the fall deposits  
551 of the IHV are compatible with fallout from unsteady eruption plumes. The SW volcano most closely  
552 resembles a scoria cone with a preserved crater width of  $W_{cr}=0.4W_{co}$  (cone width), comparable to  
553 scoria cones, but a cone height of  $H_{co}=0.1W_{co}$ . The latter is half that expected for scoria cones  
554 ( $H_{co}=0.18W_{co}$ , Wood 1980). Mean bedding dips below the critical angle of repose may result from  
555 wind-sheared volcanic plumes blown towards the northwest by trade winds, or, given the small size of  
556 the IHV, from scoria cone-forming eruptions that aborted before pyroclasts had built up to the critical  
557 angle of repose (e.g., McGetchin et al. 1974). We infer that the effusive stages of the IHV represent  
558 eruptions driven by ascent of gas-poor magma toward the ends of the eruptions.

559 There are similarities between the IHV and small volcanoes in the Lake Natron-Engaruka  
560 monogenetic volcanic field, Northern Tanzania (Dawson and Powell 1969; Mattsson and Tripoli 2011).  
561 These volcanoes, which are olivine melilitite to nephelinite in composition, exhibit morphologies  
562 comparable to tuff rings, tuff cones, maars and scoria cones. Despite the similarities with small  
563 phreatomagmatic volcanoes, the pyroclastic deposits of the maar-type volcanoes exhibit textural  
564 evidence inferred to result from dry (i.e., not phreatomagmatic) fragmentation and deposition. Mattsson  
565 and Tripoli (2011) concluded that the eruptions may have instead been magmatic and driven by the  
566 high volatile contents of the melilititic melts. Similar arguments have been put forward for kimberlite  
567 eruptions (e.g., Sparks et al. 2006).

568 The deposits and volcanoes at Igwisi Hills thus share characteristics with both small  
569 phreatomagmatic volcanoes (bedding dips, a sunken crater and lithic-rich bedded pyroclastic deposits)  
570 and with scoria cones (juvenile-rich deposits, moderately poor to good sorting). Small monogenetic  
571 eruptions can be complex and flip between phreatomagmatic and magmatic activity. Early  
572 phreatomagmatic phases can exhaust surface or ground water or build edifices that block water access  
573 to the vent—later phases are magmatic (e.g., Phases 2 and 3 at the IHV). This is a scenario that would

574 fit the evidence at Igwisi, although we note that the deposits lack evidence for wet deposition and  
575 phreatomagmatic explosions (e.g., fine ash layers, ash aggregates, large ballistic blocks).  
576

### 577 **Comparison with ancient kimberlite volcanoes**

578 The IVH are small in comparison to many well-studied kimberlite pipes, whose craters can exceed 500  
579 m in diameter (e.g., Field and Scott-Smith 1999; Field et al. 2008). Few examples of the surface  
580 edifices of kimberlites volcanoes are known. The best documented are the Cretaceous Fort à la Corne  
581 kimberlites in Canada, which comprise pyroclastic cones and reworked volcanoclastic rocks emplaced  
582 in a coastal or submarine environment (e.g., Leckie et al. 1997; Berryman et al. 2004; Pittari et al.  
583 2008; Berryman et al. 2004). They are presently buried under thick glacial till. These volcanoes have  
584 been interpreted as either shallow, wide craters filled with pyroclastic rocks (Berryman et al. 2004),  
585 positive relief tephra cones and tuff rings (Leckie et al. 1997; Zonneveld et al. 2004; Kjarsgaard et al.  
586 2007, 2009), or some combination of the two (Pittari et al. 2008; Lefebvre and Kurszlaukis 2008).  
587 Seismic reflection surveys of the 169 kimberlite appear to outline a cone 50–100 m high and >1 km in  
588 diameter (e.g., Kjarsgaard et al. 2007). The near-shore setting of these volcanoes and common presence  
589 of aqueously reworked volcanoclastic beds has led many authors to infer that the eruptions were in part  
590 phreatomagmatic (Kjarsgaard et al. 2007, 2009; Pittari et al. 2008; Lefebvre and Kurszlaukis 2008).  
591 Pyroclastic deposits include those inferred to be proximal and distal magmatic fall deposits, poorly  
592 sorted debris jet deposits from wet phreatomagmatic eruptions, and coarse-grained poorly sorted  
593 proximal pyroclastic flow deposits (Kjarsgaard et al. 2009).

594 The Meso-Neoproterozoic Tokapal kimberlite, India (Mainkar et al. 2004), comprises a 2 km  
595 wide apron of weathered and buried pyroclastic rocks 70 m thick around a large crater. The pyroclastic  
596 rocks comprise fine-grained tuffs, pyroclastic breccias with abundant lithic clasts and stratified lapilli-  
597 tuffs in which stratification is defined by lithic clast abundance. They are interpreted as pyroclastic  
598 density current deposits and pyroclastic fall deposits and appear to form an eroded low, broad tephra  
599 ring akin to a tuff ring. The Tokapal deposits overlie marine limestones and shales but may have been  
600 erupted subaerially following uplift (Mainkar et al. 2004).

601 The pyroclasts of the IHV pyroclastic rocks are morphologically similar to those found in the  
602 kimberlite tephra cones discussed above, in ancient kimberlite pipes (e.g., Mitchell 1986; Moss et al.,  
603 2011) and other ultrabasic volcanoes (e.g., kamafugite diatremes, Junqueira-Brod et al. 2004). For  
604 example, pyroclastic rocks of the Fort à la Corne kimberlites contain variable amounts of dense to  
605 poorly vesicular irregular-shaped clasts, pelletal clasts and free olivine crystals (e.g., Zonneveld et al.  
606 2004; Lefebvre and Kurszlaukis 2008; Kjarsgaard et al. 2009). Spherical droplet-shaped and irregular-  
607 shaped pyroclasts (Fig. 5A and D) and pelletal clasts result from the disruption of low viscosity  
608 magma, while the angular and poorly vesicular juvenile clasts (Fig. 5B and C) suggest fragmentation of  
609 higher viscosity magma that had already undergone some degree of groundmass crystallization and  
610 glass formation.

611 Occurrences of kimberlite lavas are rare due to erosion and few have been documented (e.g.,  
612 Mainkar et al. 2004; Skinner and Marsh 2004; Eley et al. 2008). Eley et al (2008) report intersections  
613 of igneous-textured kimberlite encountered at shallow levels in Angola. One body, which was also  
614 imaged by geophysical methods, was interpreted as a 200 m wide × 1000 m long, 3 m thick extra crater  
615 lava flow. The other was a >130 m thick coherent kimberlite unit interpreted as a lava lake. Rocks  
616 interpreted to be extra-crater lava flows at the Tokapal kimberlite, India, are heavily weathered and  
617 only encountered in drill core (Mainkar et al. 2004). Van Straaten et al (2011) interpreted a high-level  
618 body of igneous-textured kimberlite in the Victor pipe, Canada, as a lava lake. This supports our  
619 interpretation of lava lakes in the IHV.

620  
621 ***Subsurface plumbing at the IHV***

622 The dimensions of the IHV conduits and the volume of material contained within them remain largely  
623 unconstrained (Fig. 13). Surface crater radii of >50–100 m (Fig. 2) constrain the maximum diameters  
624 of any conduits, but the vertical extent and shape of the conduits (whether pipes or dikes) remains  
625 unknown. In ancient kimberlite pipes and other diatremes pipe walls are typically oriented inward at  
626 angles of 70–90°, with average dips of 82–85° inferred for kimberlite pipes (Hawthorne 1975; White  
627 and Ross 2011). Using these average values, hypothetical kimberlite pipes would extend 300–500 m  
628 beneath the central and SW volcanoes and 600–900 m beneath the NE volcano. This can be tested by  
629 estimating the minimum volume of excavated country rock obtained by calculating the volume of lithic  
630 clasts within the pyroclastic deposits. The oldest pyroclastic deposits contain the largest volumes of  
631 lithic clasts (Phase 1) and the general absence of lithic clasts in later products (Phases 2 and 3) indicates  
632 that subsurface conduits were not substantially enlarged after the early phase. The volume of these  
633 pyroclastic deposits is not well constrained, but for the NE Volcano, generously assuming that they  
634 originally formed a circular apron that was 10 m thick at the crater edge and that thinned to zero at 300  
635 m distance, then the tuffs have a minimum volume of  $2 \times 10^6 \text{ m}^3$ . If basement clasts account for on  
636 average 15 vol. % of the deposits, then the minimum volume of excavated country rock is  $3 \times 10^5 \text{ m}^3$ .  
637 This volume is roughly equivalent to either a cone with a radius of 50 m and a depth of ~110 m, or a 3  
638 m widening of a dike segment 200 m long and 500 m deep. This calculation assumes that large  
639 volumes of fragmented country rock were not dispersed widely during the eruption and do not remain  
640 trapped in the conduit. Comparisons with other kimberlite pipes suggest that the trapped volume should  
641 account for <<50 vol. % of a pipe's volume (Sparks et al., 2006). These first order estimates of  
642 excavated country rock do not imply that there are substantial conduits beneath the IHV Volcano.  
643 Although deposits of the opening phases of the eruptions are not exposed, the absence of granite-rich  
644 pyroclastic breccias mantling deposits of older, neighbouring volcanoes suggests that any explosive  
645 cratering (e.g., Sparks et al., 2006) was minimal at the IHV. These estimates suggest small conduits  
646 comparable in dimensions to those beneath scoria cones (e.g., Doubik and Hill, 1999; Keating et al.  
647 2008; Valentine 2012; Fig. 13). Future research at Igwisi should combine geophysical studies  
648 (resistivity, gravity and magnetic surveys) with rock drilling to constrain the subsurface plumbing  
649 system.

650

### 651 **Duration of IHV eruptions**

652 Minimum erupted volumes of  $\sim 10^6 \text{ m}^3$  for the IHV are at the lower end of estimates based on pipe  
653 volumes for kimberlite eruptions (Sparks et al. 2006) and are consistent with their small crater  
654 diameters and edifice dimensions. We infer that the IHV were formed by small volume, monogenetic  
655 eruptions of kimberlitic magma that ascended along a NE–SW oriented dike(s) (Fig. 13). The eruptions  
656 probably persisted for several days up to several months (comparable to monogenetic basaltic  
657 eruptions) and concluded with effusive phases that each lasted for several hours to days.

658

### 659 **Conclusions**

660 The three Igwisi Hills volcanoes, Tanzania, are the only examples of kimberlite volcanoes that still  
661 have surface constructs preserved on the Earth's surface. Cosmogenic  $^3\text{He}$  exposure dating of olivine in  
662 the lavas gives Upper Pleistocene/Holocene eruption ages. This age is supported by palaeomagnetic  
663 analyses and confirms them as the youngest known kimberlite bodies. Such young eruption ages may  
664 indicate that the Tanzanian craton is undergoing a new phase of kimberlitic volcanism and more  
665 eruptions of kimberlitic magma may be expected in the future. The three small volcanoes comprise  
666 pyroclastic edifices, craters and lavas and were generated by small-volume (VEI 2), monogenetic  
667 eruptions of kimberlite magma that reached the Earth's surface along a NE–SW-oriented dike or dikes  
668 (Fig. 13). The pyroclastic cones are comprised of diffusely bedded fall deposits and pyroclasts include  
669 vesicular scoriaceous clasts, pelletal clasts and dense juvenile clasts. Bedding and pyroclast

670 characteristics are consistent with repetitive small explosions. Pyroclasts are similar in size and  
671 morphology to those commonly found in other kimberlite rocks indicating overlap in magma  
672 fragmentation dynamics between the Igwisi eruptions and those recorded by ancient kimberlite pipes.  
673 The morphology and physical features of the lavas indicate unexpectedly high lava viscosity, probably  
674 as a result of degassing and partial groundmass crystallization of the magma at shallow depth. Each  
675 volcano broadly shows the same three eruptive phases: 1) early vent-clearing explosive eruptions  
676 comprising elevated quantities of fragmented country rock, and that may have been drive by  
677 phreatomagmatic explosions; 2) lower-intensity juvenile-rich explosive eruptions that generated weak  
678 eruption columns that were sheared by dominant trade winds from the east and south-east (Fig. 13), and  
679 that constructed pyroclastic edifices around the vents and; 3) waning-stage effusions of degassed and  
680 partially crystallised viscous lava. These are comparable to eruption pathways observed at, and inferred  
681 for, many eruptions of other types of magmas.

### 682 683 **Acknowledgements**

684 We dedicate this paper to Barry Dawson—the last geologist to visit the volcanoes in 1966—as thanks  
685 for his great encouragement, advice and help and for many fruitful discussions throughout this study.  
686 Field and laboratory studies were supported a National Geographic Committee on Research and  
687 Exploration grant (no. 8562\_08) awarded to RJB, the Natural Environment Research Council  
688 Geophysical Equipment Facility (grant no. 894) and the Royal Society International Travel Grant  
689 scheme. RSJS acknowledges support from a European Research Council Advanced grant. Alan Hobbs  
690 and Colin Kay at GEF are thanked for training and support. We thank Craig Storey and Dan Condon  
691 for advice on radiometric dating. We are indebted to Rod Smith of Cranbrook School, Kent, Mama  
692 Kisinga and the Friends of Urambo and Mwanhala charity for logistical support, lodgings, help and  
693 advice. We thank Urambo district council and the villagers at Igwisi for permission to work at the  
694 volcanoes. Bruce Kjarsgaard, Pierre-Simon Ross and Greg Valentine are thanked for expert reviews  
695 that greatly improved the manuscript. James White is thanked for editorial input and discussion.

### 696 697 **References**

- 698 Bassett H (1954). The Igwisi craters and lavas. *Rec Geol Surv Tanganyika* 4:81–92.
- 699
- 700 Batumike JM, Griffin, WL, Belousova NJ, Pearson NJ, O'Reilly SY, Shee SR (2008). LAM-ICPMS  
701 U-Pb dating of kimberlitic perovskite: Eocene–Oligocene kimberlites from the Kundelungu Plateau,  
702 D.R. Congo. *Earth Planet Sci Lett* 267:609–619.
- 703
- 704 Bell K, Dodson MH (1981). The geochronology of the Tanzanian shield. *J Geol* 89:109–128.
- 705
- 706 Berryman A, Scott Smith BH, Jellicoe B (2004). Geology and diamond distribution of the 140/141  
707 kimberlite, Fort à la Corne, central Saskatchewan, Canada. *Lithos* 76:99–114.
- 708
- 709 Brown RJ, Buse B, Sparks RSJ, Field M (2008a). On the welding of pyroclasts from very low-  
710 viscosity magmas: Examples from kimberlite volcanoes. *J Geol* 116:354–374.
- 711
- 712 Brown RJ, Gernon T, Steifenhof, Field M (2008b). Geological constraints on the eruption of the  
713 Jwaneng central kimberlite pipe, Botswana. *J Volcanol Geotherm Res* 174:195–208.
- 714
- 715 Brown RJ, Tait M, Field M, Sparks RSJ (2009). Geology of a complex kimberlite pipe (K2 pipe,  
716 Venetia mine, South Africa): Insights into conduit processes during explosive ultrabasic eruptions. *Bull*  
717 *Volcanol* 71:95–112.

718  
719 Buisman I, Sparks RSJ, Manya S, Brown RJ, Kavanagh J, Walter MJ, submitted. Olivine chemistry of  
720 exceptionally young (Holocene) kimberlite of the IHV, Tanzania. *Contrib Min Pet*.  
721  
722 Buse B, Schumacher JC, Sparks RSJ, Field M (2010). Growth of bultfonteinite and hydrogarnet in  
723 metasomatized basalt xenoliths in the B/K9 kimberlite, Damtshaa, Botswana: insights into  
724 hydrothermal metamorphism in kimberlite pipes. *Contrib Min Pet* 160:533–550.  
725  
726 Cas RAF, Wright JV (1987). *Volcanic Successions*. Chapman and Hall, London p. 528.  
727  
728 Cas RAF, Hayman P, Pittari A, Porritt L (2008). Some major problems with existing models and  
729 terminology associated with kimberlite pipes from a volcanological perspective, and some suggestions.  
730 *J Volcanol Geotherm Res* 174:209–225.  
731  
732 Castrucchio A, Rust A, Sparks RSJ (2010). Rheology and flow of crystal-rich bearing lavas: insights  
733 from analogue gravity currents. *Earth Planet Sci Lett* 297:471–480.  
734  
735 Davis GL (1977). The ages and uranium contents of zircons from kimberlites and associated rocks.  
736 *Carnegie Institute Washington*. 76:631–635.  
737  
738 Dawson JB (1964). Carbonate tuff cones in northern Tanganyika. *Geol Mag* 101:129–137.  
739  
740 Dawson JB (1971). *Advances in Kimberlite Geology*. *Earth Sci Rev* 7:187–214.  
741  
742 Dawson JB (1994). Quaternary kimberlitic volcanism on the Tanzania craton. *Contrib Min Pet*  
743 116:473–485.  
744  
745 Dawson JB, Powell DG (1969). The Natron-Engaruka explosion crater area, Northern Tanzania, *Bull.*  
746 *volcanol.*33:761–817.  
747  
748 Dawson JB, Hawthorne JB (1973). Magmatic sedimentation and carbonatitic differentiation in  
749 kimberlite sills at Benfontein, South Africa. *J Geol Soc London* 129:61–85.  
750  
751 Doubik P, Hill BE (1999). Magmatic and hydromagmatic conduit development during the 1975  
752 Tolbachik Eruption, Kamchatka, with implications for hazards assessment at Yucca Mountain, NV. *J*  
753 *Volcanol Geotherm Res* 91:43–64.  
754  
755 Douce AEP, Beard JS (1994). Dehydration melting of biotite gneiss and quartz amphibolite from 3 to  
756 15 kbar. *J Pet* 36:707–738.  
757  
758 Dunai TJ (2000). Scaling factors for production rates of in situ produced cosmogenic nuclides: a  
759 critical reevaluation. *Earth Planet Sci Lett* 176:157–169.  
760  
761 Eley R, Grütter H, Louw A, Tunguno C, Twidale J (2008). Exploration Geology of the Luxinga  
762 Kimberlite Cluster (Angola) with Evidence Supporting the Presence of Kimberlite Lava. Extended  
763 Abstract 9th Int. Kimberlite Conf.  
764

765 Field M, Gibson JG, Wilkes TA, Gababotse J, Khutjwe P (1997). The geology of the Orapa A/K1  
766 Kimberlite, Botswana: further insight into the emplacement of kimberlite pipes. In: Dobretsov NL,  
767 Goldin SV, Kontorovich AE, Polyakov GV, Sobolev NV (Eds), Proceedings of the Sixth International  
768 Kimberlite Conference 1: Kimberlites, Related Rocks and Mantle Xenoliths. Russian Geology and  
769 Geophysics, Novosibirsk, Russia, 24–39.  
770

771 Field M, Scott Smith BH (1999). Contrasting geology and near–surface emplacement of kimberlite  
772 pipes in southern Africa and Canada. In: Gurney, J., Gurney, J., Pascoe, M., Richardson, S. (Eds.), J.B.  
773 Dawson Volume. Proceedings of the VIIth International Kimberlite Conference. Vol. 1. Red Roof  
774 design cc, Cape Town 214–237.  
775

776 Field M, Stiefenhofer J, Robey J, Kurszlaukis S (2008). The kimberlite–hosted diamond deposits of  
777 southern Africa: a review. *Ore Geology Reviews* 34:33–75.  
778

779 Fisher RV, Schmincke H-U (1984). *Pyroclastic Rocks*. Springer-Verlag, Berlin, New York, 1984.  
780

781 Foeken JPT, Persano C, Stuart FM, ter Voorde M. (2007). Role of topography in isotherm perturbation:  
782 Apatite (U-Th)/He and fission track results from the Malta tunnel, Tauern window, Austria. *Tectonics*  
783 26.  
784

785 Fontana GPG, Mac Niocaill C, Brown RJ, Sparks RSJ, Field M (2011). Emplacement temperatures of  
786 pyroclastic and volcanoclastic deposits in kimberlite pipes in southern Africa. *Bull Volcanol* 73:1063–  
787 83  
788

789 Fozzard PMH (1956). Further notes on the volcanic rocks from Igwisi, Tanganyika. *Rec Geol Surv*  
790 Tanganyika, 6:69–75.  
791

792 Gernon T, Gilbertson M, Sparks RSJ, Field M (2008a). Gas-fluidisation in an experimental tapered  
793 bed: Insights into processes in diverging volcanic conduits. *J Volcanol Geotherm Res* 174:49–56.  
794

795 Gernon T, Sparks RSJ, Field M (2008b). Degassing structures in volcanoclastic kimberlite: examples  
796 from southern African pipes. *J Volcanol Geotherm Res* 174:186–194.  
797

798 Gernon TM, Fontana G, Field M, Sparks RSJ, Brown RJ, Mac Niocaill C (2009a). Pyroclastic flow  
799 deposits from a kimberlite eruption: the Orapa south crater, Botswana. *Lithos*, 112:566–578.  
800

801 Gernon TM, Fontana G, Field M, Sparks RSJ (2009b). Depositional processes in a kimberlite crater:  
802 the Upper Cretaceous Orapa South Pipe (Botswana). *Sedimentology* 56:623–643.  
803

804 Gobba JM (1989). Kimberlite exploration in Tanzania. *J African Earth Sci* 9 314:565–578.  
805

806 Goehring BM, Kurz MD, Balco G, Schaefer JM, Licciardi J, Lifton NA (2010). Reevaluation of in situ  
807 cosmogenic (3)He production rates. *Quat Geochron* 5:410–418.  
808

809 Haggerty SE, Raber E, Naeser CW (1983). Fission track dating of kimberlite zircons. *Earth and*  
810 *Planetary Science Letters* 63: 41–50.  
811

812 Hawthorne JB (1975). Model of a kimberlite pipe. *Phys Chem Earth* 9:1–15

813  
814 Hon K, Kauahikaua J, Denlinger R, Mackay K (1994). Emplacement and inflation of pāhoehoe sheet  
815 flows: observations and measurements of active lava flows on Kilauea volcano, Hawai‘i. *Geol Soc Am*  
816 *Bull*106:351–370  
817  
818 Junqueira–Brod TC, Brod JA, Gaspar JC, Jost H (2004). Kamafugitic diatremes: Facies  
819 characterisation and genesis—examples from the Goiás alkaline province, Brazil. *Lithos* 76:261–282.  
820  
821 Keating GN, Valentine GA, Krier DJ, Perry FV (2008) Shallow plumbing systems for small-volume  
822 basaltic volcanoes. *Bull Volcanol* 70:563–582.  
823  
824 Kjarsgaard BA (2007). Kimberlite diamond deposits, in Goodfellow WD, Ed, *Mineral Deposits of*  
825 *Canada: A Synthesis of Major Deposit Types, District Metallogeny, the Evolution of Geological*  
826 *Provinces, and Exploration Methods: Geological Association of Canada, Mineral Deposits Division,*  
827 *Special Publication 5:245–272.*  
828  
829 Kjarsgaard BA, Leckie DA, Zonneveld J–P (2007). Discussion of “Geology and diamond distribution  
830 of the 140/141 kimberlite, Fort à la Corne, central Saskatchewan, Canada” by Berryman AK, Scott  
831 Smith BH, Jellicoe BC (*Lithos*76:99–114). *Lithos* 97:422–428.  
832  
833 Kjarsgaard BA, Harvey S, McClintock M, Zonneveld JP, Du Plessis P, McNeil D, Heaman L (2009).  
834 Geology of the Orion South kimberlite, Fort à la Corne, Canada. *Lithos* 1125:600–617.  
835  
836 Kurszlauskis S, Barnett WP (2003) Volcanological and structural aspects of the Venetia Kimberlite  
837 cluster – a case study of South African kimberlite maar-diatreme volcanoes *South African J Earth Sci*  
838 *106: 165–192.*  
839  
840 Kurszlauskis S, Lorenz V (2008). Formation of “Tuffisitic Kimberlite” by phreatomagmatic processes. *J*  
841 *Volcanol Geotherm Res* 174:68–80.  
842  
843 Kurz MD, Colodner D, Trull TW, Sampson DE (1987). Exposure age dating with cosmogenic<sup>3</sup>He:  
844 Influence of the Earth's magnetic field. *EOS*, 68:1286.  
845  
846 Leckie DA, Kjarsgaard BA, Bloch J, McIntyre D, McNeil D, Stasiuk L, Heaman L (1997).  
847 Emplacement and reworking of Cretaceous, diamond-bearing, crater facies kimberlite of central  
848 Saskatchewan, Canada. *Geol Soc Am Bull* 109:1000–1020.  
849  
850 Lefebvre N, Kurszlauskis S (2008). Contrasting eruption styles of the 147 kimberlite, Fort à la Corne,  
851 Saskatchewan, Canada. *J Volcanol Geotherm Res* 174:171–185.  
852  
853 Lipman PW, Banks NG (1987). ‘A’ā flow dynamics, Mauna Loa 1984. *US Geol Surv Prof Paper*  
854 *1350:1527–1567*  
855  
856 Lorenz V (1975). Formation of phreatomagmatic maar-diatreme volcanoes and its relevance to  
857 kimberlite diatremes. *Phys. Chem. Earth* 9:17–27.  
858  
859 Lorenz V (2007). Syn- and post-eruptive hazards of maar-diatreme volcanoes. *J Volcanol Geotherm*  
860 *Res* 159:285–312.

861  
862 Lorenz V, Kurszlaukis S (2007). Root zone processes in the phreatomagmatic pipe emplacement model  
863 and consequences for the evolution of maar-diatreme volcanoes. *J Volcanol Geotherm Res* 159:4–32.  
864  
865 Macdonald GA (1953). Pāhoehoe, ‘a’ā and block lava. *Am J Sci* 215:169–191  
866  
867 Mainkar D, Lehmann B, Haggerty SE (2004). The crater–facies kimberlite system of Tokapal, Bastar  
868 district, Chhattisgarh, India. *Lithos*, 76:201–217.  
869  
870 Mattsson HB, Tripoli BA (2011). Depositional characteristics and volcanic landforms in the lake  
871 Natron-Engaruka monogenetic field, northern Tanzania. *J Volcanol Geotherm Res* 203:23–34.  
872  
873 McClintock M, White JDL, Houghton BF, Skilling IP (2008). Physical volcanology of a large crater-  
874 complex formed during the initial stages of Karoo flood basalt volcanism, Sterkspruit, Eastern Cape,  
875 South Africa. *J Volcanol Geotherm Res* 172:93-111.  
876  
877 McGetchin TR, Settle M, Chouet BA (1974). Cinder Cone Growth Modeled After Northeast Crater,  
878 Mount Etna, Sicily. *J Geophys Res* 79:3257-3272.  
879  
880 Mitchell RH (1970). Kimberlite and related rocks – a critical reappraisal. *J Geol* 78:686–704.  
881  
882 Mitchell RH (1986). Kimberlites. *Mineralogy, Geochemistry and Petrology*. Plenum Press 442p.  
883  
884 Mitchell RH (2008). Petrology of hypabyssal kimberlites: relevance to primary magma compositions. *J*  
885 *Volcanol Geotherm Res* 174:1–8.  
886  
887 Moss S, Russell JK, Andrews GDM (2008) Progressive infilling of a kimberlite pipe at Diavik,  
888 Northwest Territories, Canada: Insights from volcanic facies architecture, textures, and granulometry. *J*  
889 *Volcanol Geotherm Res* 174:103-116.  
890  
891 Moss S, Russell JK (2011). Fragmentation in kimberlite: products and intensity of explosive eruptions.  
892 *Bull Volcanol* 72:983–1003.  
893  
894 Newhall CG, Self S (1982). The volcanic explosivity index (VEI): An estimate of explosive magnitude  
895 for historical volcanism. *J Geophys Res* 87:123–1238.  
896  
897 Pirrung M, Büchel G, Lorenz V, Treutler H- (2008). Post–eruptive development of the Ukinrek east  
898 maar since its eruption in 1977 A.D. in the periglacial area of south–west Alaska. *Sedimentology* 55:  
899 305–334.  
900  
901 Pittari A, Cas RAF, Lefebvre N, Robey J, Kurszlaukis S, Webb K (2006). Eruption processes and  
902 facies architecture of the Orion central kimberlite volcanic complex, Fort a la Corne, Saskatchewan;  
903 kimberlite mass flow deposits in a sedimentary basin. *J Volcanol Geotherm Res* 174:152–170.  
904  
905 Porritt LA, Cas R, Crawford BB (2008). In-vent column collapse as an alternative model for massive  
906 volcanoclastic kimberlite emplacement: an example from the Fox kimberlite, Ekati Diamond Mine,  
907 NWT, Canada. *J Volcanol Geotherm Res* 174:90–102.  
908

909 Porritt LA, Russell JK (in press). Kimberlite ash: fact or fiction? *Phys Chem Earth*.  
910  
911 Porter SC (1972). Distribution, Morphology, and Size Frequency of Cinder Cones on Mauna Kea  
912 Volcano, Hawaii. *Geol Soc Am Bull* 83:3607-3612.  
913  
914 Reid AM, Donaldson CH, Dawson JB, Brown RW, Ridley WI (1975). The Igwisi Hills extrusive  
915 "kimberlites". *Phys Chem Earth* 9:199–218.  
916  
917 Ross P–S, White JD (2006). Debris jets in continental phreatomagmatic volcano: A field study of their  
918 subterranean rocks in the Coombs Hills vent complex, Antarctica. *J Volcanol Geotherm Res* 149:62–  
919 84.  
920  
921 Ross P–S, Delpit S, Haller MJ, Németh K, Corbella H (2011). Influence of the substrate on maar-  
922 diatreme volcanoes—an example of a mixed setting from the Pali Aike volcanic field, Argentina. *J*  
923 *Volcanol Geotherm Res* 201:253–271.  
924  
925 Rowland SK, Walker GPL (1988). Mafic-crystal distributions, viscosities, and lava structures of some  
926 Hawaiian lava flows. *J Volcanol Geotherm Res* 35:55–66.  
927  
928 Sampson DN (1953). The volcanic hills at Igwisi. *Rec Geol Surv Tanganyika* 3:48–53.  
929  
930 Skinner EMW, Marsh JS (2004). Distinct kimberlite pipe classes with contrasting eruption processes.  
931 *Lithos* 76:183-200.  
932  
933 Sparks RSJ, Baker L, Brown RJ, Field M, Schumacher J, Stripp G (2006). Dynamical constraints on  
934 kimberlite volcanism. *J Volcanol Geotherm Res* 155:18–48.  
935  
936 Stiefenhofer J, Farrow DJ (2004). Geology of the Mwadui kimberlite, Shinyanga district, Tanzania.  
937 *Lithos*, 76:139–160.  
938  
939 Stripp GR, Field M, Schumacher JC, Sparks RSJ (2006). Post-emplacement serpentinization and related  
940 hydrothermal metamorphism in a kimberlite from Venetia, South Africa. *J Met Geology* 24: 515–534  
941  
942 Valentine GA (2012). Shallow plumbing systems for small-volume basaltic volcanoes, 2: evidence  
943 from crustal xenoliths at scoria cones and maars. *J Volcanol Geotherm Res*.  
944  
945 Valentine GA, Groves KR (2008). Entrainment of country rock during basaltic eruptions of the Lucero  
946 volcanic field, New Mexico. *J Geol* 104:71–90.  
947  
948 Van Straaten BI, Kopylova MG, Russell JK, Scott Smith BH (2011). A rare occurrence of a crater-  
949 filling clastogenic extrusive coherent kimberlite, Victor Northwest (Ontario, Canada). *Bull Volcanol*  
950 73:1047–1062.  
951  
952 Walker GPL(1973). Lengths of lava flows. *Phil Trans Roy Soc London*. 274:107–118.  
953  
954 Walker GPL(1991). Structure, and origin by injection of lava under surface crust, of tumuli, "lava  
955 rises", "lava-rise pits", and "lava-inflation clefts" in Hawaii. *Bull Volcanol* 53: 546–558.  
956

957 Walters AL, Phillips JC, Brown RJ, Field M, Gernon T, Stripp G(2006). The role of fluidisation in the  
958 formation of volcanoclastic kimberlite: Grain size observations and experimental investigation. *J*  
959 *Volcanol Geotherm Res* 155:119–137.  
960  
961 White JDL, Houghton BF (2006). Primary volcanoclastic rocks. *Geology* 34:677–680.  
962  
963 White JDL, Ross P–S(2011). Maar-diatreme volcanoes: A review. *J Volcanol Geotherm Res* 201:1–29.  
964  
965 Willcox A, Buisman I, Sparks RSJ, Brown RJ, Manya S, Schumacher JS, Tuffen H (submitted).  
966 Petrology, geochemistry and low-temperature alteration of extrusive lavas and pyroclastic rocks of the  
967 Igwisi Hills kimberlites, Tanzania. *Chem Geol*.  
968  
969 Williams AJ, Stuart FM, Day SJ, Phillips WM (2005). Using pyroxene microphenocrysts to determine  
970 cosmogenic <sup>3</sup>He concentrations in old volcanic rocks: an example of landscape development in central  
971 Gran Canaria. *Quat Sci Rev* 24:211–222.  
972  
973 Wohletz KH, Sheridan MF (1983). Hydrovolcanic explosions II. Evolution of basaltic tuff rings and  
974 tuff cones. *Am J Sci* 283:385–413.  
975  
976 Wood CA (1980). Morphometric evolution of cinder cones. *J Volcanol Geotherm Res* 7:387–413.  
977  
978 Zonneveld J-P, Kjarsgaard BA, Harvey SE, Heaman LM, McNeil DH, Marcia KY (2004).  
979 Sedimentologic and stratigraphic constraints on the emplacement of the Star kimberlite east–central  
980 Saskatchewan. *Lithos* 76:115–138.

981  
982 **Figure captions**

983 **Figure 1.** Geological sketch map of the Tanzanian Craton. The IHV (4°53'19.22"S, 31°55'59.15"E)  
984 are situated on the western side of the craton, northwest of the village of Igwisi.  
985

986 **Figure 2.** Geological and topographic map of the IHV. Insets show histograms of beddings dips in  
987 pyroclastic edifices and profiles of the three volcanoes.  
988

989 **Figure 3.** Photographs of the three volcanoes. A) Cosmogenic sample site for IH15 (top of lava in NE  
990 volcano). B) Cosmogenic sampling site for IH52 (foot wall scarp in NE volcano lava developed during  
991 magma late-stage crater subsidence). C) The NE volcano, showing the flat crater floor, the northern  
992 crater wall comprised of pyroclastic rocks, and the lavas on the eastern side. View looking north from  
993 the central volcano. D) Central volcano showing the partial pyroclastic cone on the west of the volcano  
994 and the lava coulee that fills the inferred central volcano crater and has partially filled the NE volcano's  
995 crater. View looking south from the northern margin of the NE volcano. E) The SW volcano showing  
996 the pyroclastic cone and central crater. The western side of the cone is 12 m higher than the eastern  
997 side. View towards the south from the central volcano.  
998

999 **Figure 4.** Graphic summary log through pyroclastic deposits of the northern crater wall of the NE  
1000 volcano. Photographs show: A) centimeter-scale bedding defined by variations in abundance of lithic  
1001 clasts; B) close-up of A showing lithic lapilli of basement granite and gneiss; C) Close up of A showing  
1002 clast-supported nature of juvenile and lithic lapilli.  
1003

1004 **Figure 5.** Transmitted light thin-section photographs of pyroclastic lithofacies of the IHV (see Table  
1005 3). A) Lithic-bearing lapillistone (bL) from the NE volcano. Accidental clasts comprise crystals and  
1006 rock fragments derived from the basement. ~50 cm shown on rule. Dense juvenile lapilli have  
1007 amoeboid outlines or are pelletal lapilli. B) Juvenile-rich lapillistone comprised of poorly vesicular  
1008 lapilli and ash-grade juvenile clasts with irregular outlines (central volcano). C) Close-up of vesicular  
1009 juvenile lapilli in B. D) Extracted pelletal lapilli from the pelletal-clast-rich lapillistone shown in Figure  
1010 4C. E) Centimetre-scale stratification within juvenile-rich lapillistone and tuffs from the SW volcano.  
1011 Comprised predominantly of amoeboid dense to poorly vesicular juvenile clasts.

1012  
1013 **Figure 6.** Juvenile-rich pyroclastic lithofacies of the IHV (see Table 3). A) Coarse-grained scoria fall  
1014 deposit (bL) overlain by coarse tuff. Centimetre divisions on rule. B) weakly bedded juvenile rich  
1015 pyroclastic (bL) on inner crater wall of central volcano. 10 cm divisions on metre-rule. C) Bedded  
1016 juvenile-rich lapillistone with scattered dense juvenile coarse lapilli. Centimetre divisions on rule. D)  
1017 Close-up of bedded juvenile-rich lapillistone in d. Bedding is defined by grain size. E) Rare lithic block  
1018 in juvenile-rich lapillistone, central volcano. 10 cm divisions on rule. F) Bedded pelletal-clast-rich  
1019 lapillistone (bpell) from the NE volcano. Rock is comprised predominantly of clast-supported pelletal  
1020 lapilli.

1021  
1022 **Figure 7.** Graphic summary log (left) and photographs of polished slabs (centre) up through the lava  
1023 flow of the NE volcano. Olivine crystals are concentrated in the lower third and vesicles are restricted  
1024 to the upper third. Transmitted light photographs of thin-sections through the lava (right).

1025  
1026 **Figure 8.** The lava coulee of the central volcano. A) Outcrop photo showing several lapilli-sized lithic  
1027 clasts (granitic basement). B) Polished slab showing abundant ash-grade lithic clasts (light) and olivine  
1028 crystals (dark).

1029  
1030 **Figure 9.** Selected BSE images of various minerals found in IHV samples. A) Rounded xenocrystic  
1031 olivine mantled with perovskite and Mg-Al-spinel. B) Marginally resorbed phenocrystic olivine found  
1032 in the groundmass, C) Forsterite inclusion in a titanomagnetite host crystal, D) K-phlogopite with Ba-  
1033 rich-phlogopite (kinoshitalite) overgrowths, E) Apatite hopper crystals and monticellite,  
1034 F) Titanomagnetite with Cr-rich core and the Mg-Al-spinel rim replaced by hydrogarnet, G) Spongy  
1035 tabular calcite laths and amorphous calcite including a spinel pseudomorph, H) Calcite with dolomitic  
1036 patches found in tuff samples and sub-rounded apatite grains. Abbreviations: *fo* forsterite, *prv*  
1037 perovskite, *sp* spinel, *t-sp* titanomagnetite, *cal* calcite, *dol* dolomite, *phg* phlogopite, *hgt* hydrogarnet,  
1038 *mnt* monticellite, *ap* apatite, *srp* serpentine, *phenol* phenocryst, *xeno* xenocryst, Scale bars shown are  
1039 100  $\mu\text{m}$ .

1040  
1041 **Figure 10.** Selected BSE images of the groundmass mineralogy found in IHV samples. Refer to text  
1042 for details. A) IH5, a tuff sample from the central volcano; B) IH20, a lava sample from the central  
1043 volcano; C) IH30, top of NE lava flow; D) IH53, lower part of NE lava flow. Abbreviations found in  
1044 caption for Figure 8. Scale bars all 100  $\mu\text{m}$

1045  
1046 **Figure 11.** Representative orthogonal plots of thermal demagnetisation (sample PL11a) and alternating  
1047 field demagnetisation (sample PL4b) and an equal-area stereographic projection of sample-mean  
1048 directions. In the orthogonal plots solid (open) circles represent projections into the horizontal (vertical)  
1049 planes. On the stereographic projection the closed (open) symbols represent downward (upward)  
1050 directed vectors. The mean direction is marked by a cross along with cone of 95% confidence about the  
1051 mean.

1052  
 1053  
 1054  
 1055  
 1056  
 1057  
 1058  
 1059  
 1060  
 1061  
 1062  
 1063  
 1064  
 1065  
 1066  
 1067  
 1068  
 1069  
 1070  
 1071  
 1072  
 1073  
 1074  
 1075  
 1076  
 1077  
 1078  
 1079  
 1080  
 1081  
 1082  
 1083  
 1084  
 1085  
 1086  
 1087  
 1088  
 1089  
 1090  
 1091  
 1092  
 1093  
 1094  
 1095  
 1096  
 1097

**Figure 12.** Graphic summary log showing the deposits of the three main eruption phases that characterized the IVH eruptions.

**Figure 13.** Cross-sections of the IHV showing inferred structure of subsurface conduits as reconstructed from surface deposits. Insets show strong shearing of the volcanic plumes by trade winds and inferred position of NE-SW oriented dikes and craters (at pre-eruptive substrate level) for the three volcanoes. Position of cross-sections is shown. See Figure 2 for lithological key.

Sample	$^3\text{He}/^4\text{He}$ crush ( $R/R_a$ )	Melt weight (mg)	$^3\text{He}/^4\text{He}$ melt ( $R/R_a$ )	$^3\text{He}$ cos* ( $10^5$ atoms/g)	P local (atoms/g/yr)	Topographic shielding	Exposure age (ka)
--------	--	------------------------	--	--	-------------------------	--------------------------	----------------------

IH15	4.59 ± 0.06	220	4.71 ± 0.13	7.9 ± 5.7	141	0.97	5.9 ± 4.3
IH52a	4.61 ± 0.04	209	10.2 ± 7.0	10.2 ± 7.0	141	0.65	11.2 ± 7.8
IH52b	4.61 ± 0.04	191	4.82 ± 0.06	11.4 ± 4.3	141	0.65	12.4 ± 4.8
IH61	4.53 ± 0.04	198	4.73 ± 0.06	10.1 ± 3.6	141	0.96	7.6 ± 2.8

1098  
1099  
1100  
1101  
1102  
1103  
1104  
1105  
1106  
1107  
1108  
1109  
1110  
1111  
1112  
1113  
1114  
1115  
1116  
1117  
1118  
1119  
1120  
1121  
1122  
1123  
1124  
1125  
1126  
1127  
1128  
1129  
1130  
1131  
1132  
1133  
1134  
1135  
1136  
1137  
1138

**Table 1.** Results of <sup>3</sup>He cosmogenic dating of IHV lavas. IH15 is from the central volcano, all others are from the NE volcano.

	Volume (m <sup>3</sup> )		Total
	Lava	Pyroclastic	
NE volcano	377 000	>795 000	1 172 000

CE volcano	399 000	>910 000	1 309 000
SW volcano	>20 000	>995 000	1 015 000
Total			3496 000

1139  
1140  
1141  
1142  
1143  
1144  
1145  
1146  
1147  
1148  
1149  
1150  
1151  
1152  
1153  
1154  
1155  
1156  
1157  
1158  
1159  
1160  
1161  
1162  
1163  
1164  
1165  
1166  
1167  
1168  
1169  
1170  
1171  
1172  
1173  
1174  
1175  
1176  
1177  
1178

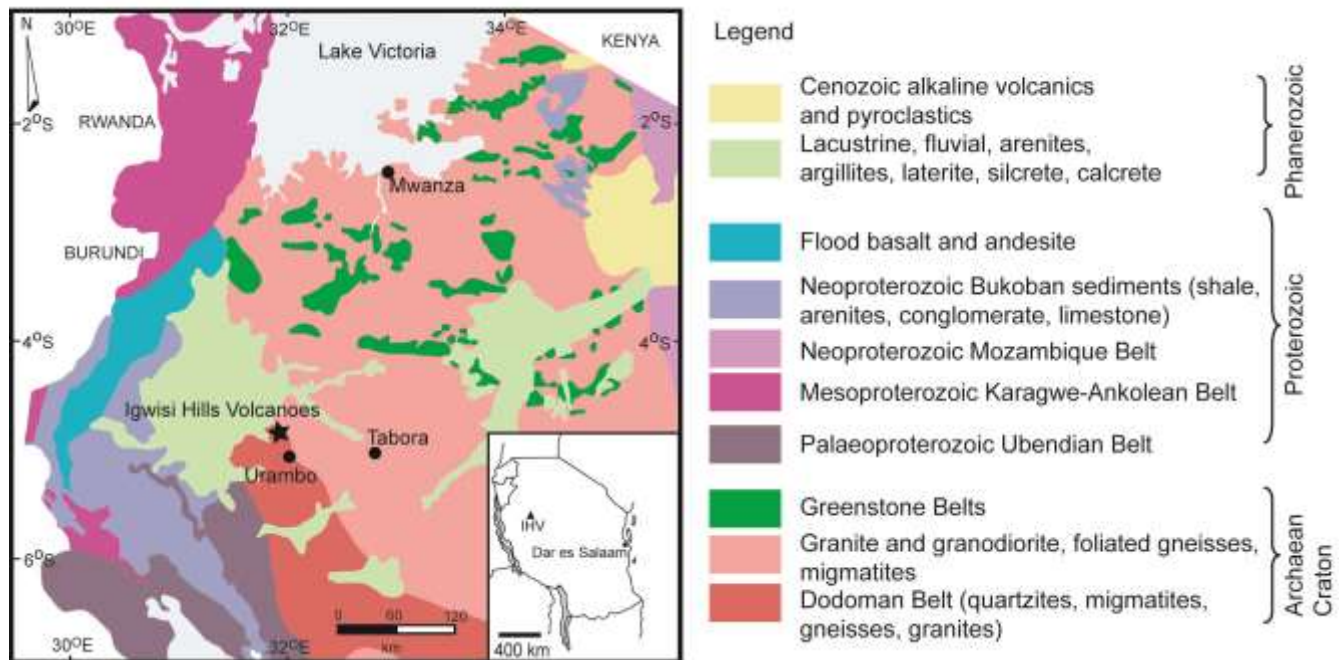
**Table 2.** Calculated volumes for preserved surface products of the IHV using xyz GPS survey data and Gemcom GEMS™ software.

<b>Lithofacies</b>	<b>Composition</b>	<b>Structure</b>
Bedded lithic-bearing coarse tuff and lapillistone (blT/blL) See Figure 4.	Clast-supported, well sorted ( $\sigma_{\phi} = 2$ ), coarse ash-and fine lapilli-grade olivine crystals, micro-xenoliths, juvenile clasts, pelletal clasts, lithic clasts and xenocrysts; non-vesicular juvenile clasts have irregular, amoeboid and spherical shapes and reach 4 mm in diameter; pelletal lapilli consist of olivine/micro-xenolith grains 0.2–2mm in diameter covered in a 0.01–0.5 mm thick coating of solidified kimberlite	Beds 2–25 cm thick; thinly bedded packages up to 1.6 m thick; defined by grain size and abundance of lithic clasts and olivine

	groundmass; lithic clasts (<10cm diameter) present in low abundances (5–12 vol.%), rarely reaching ~40 vol.% and comprise ash to lapilli-sized granite and amphibolite lithic clasts and crustal xenocrysts with tabular to equant shapes.	crystals/micro-xenoliths.
Bedded pelletal clast-rich tuff and lapillistone (bpeLT/bpeLL) See Figure 6.	Clast-supported, very well sorted ( $\sigma_{\phi}$ = 0.75–1), subspherical pelletal clasts (30–60 vol. %) and juvenile clasts (40–70 vol. %) 0.25–8 mm in diameter; pelletal clasts (as above); juvenile clasts are dense to poorly vesicular with subspherical to weakly amoeboid shapes; vesicles are spherical to elongate and coalesced, 0.01–0.5 mm in diameter and account for 5–11 vol. % of each clast; dense subspherical aphyric juvenile lapilli up to 5 cm in diameter account for <2–5 vol. % of this lithofacies.	Beds 0.5–15 cm thick; defined by sharp changes in grain size; commonly occurs interstratified with bsT/bsL.
Bedded juvenile-rich tuff and lapillistone (bT/bL) See Figure 6.	Clast-supported, well sorted ( $\sigma_{\phi}$ = 1.5–2), dense to poorly vesicular angular juvenile scoria clasts 0.5–50 mm in diameter; vesicles occur in low abundances (10–20 vol. %) are spherical to elongate in shape or coalesced and 0.02–3 mm in diameter; free olivine crystals and micro-xenoliths present in variable abundances (<15 vol. %); basement lithic clasts are rare.	Beds 3–>100 cm thick; defined by grain size; commonly occurs interstratified with bspeLT/bspeLL.
Massive to bedded juvenile clast-rich lapillistone (mbL)	Compositionally similar to bsL (above); clast-supported moderately to well sorted (estimated) scoria lapilli and coarse ash; rare lithic clasts <6 cm in diameter.	Massive to very crudely bedded on a metre-scale defined by grain size.

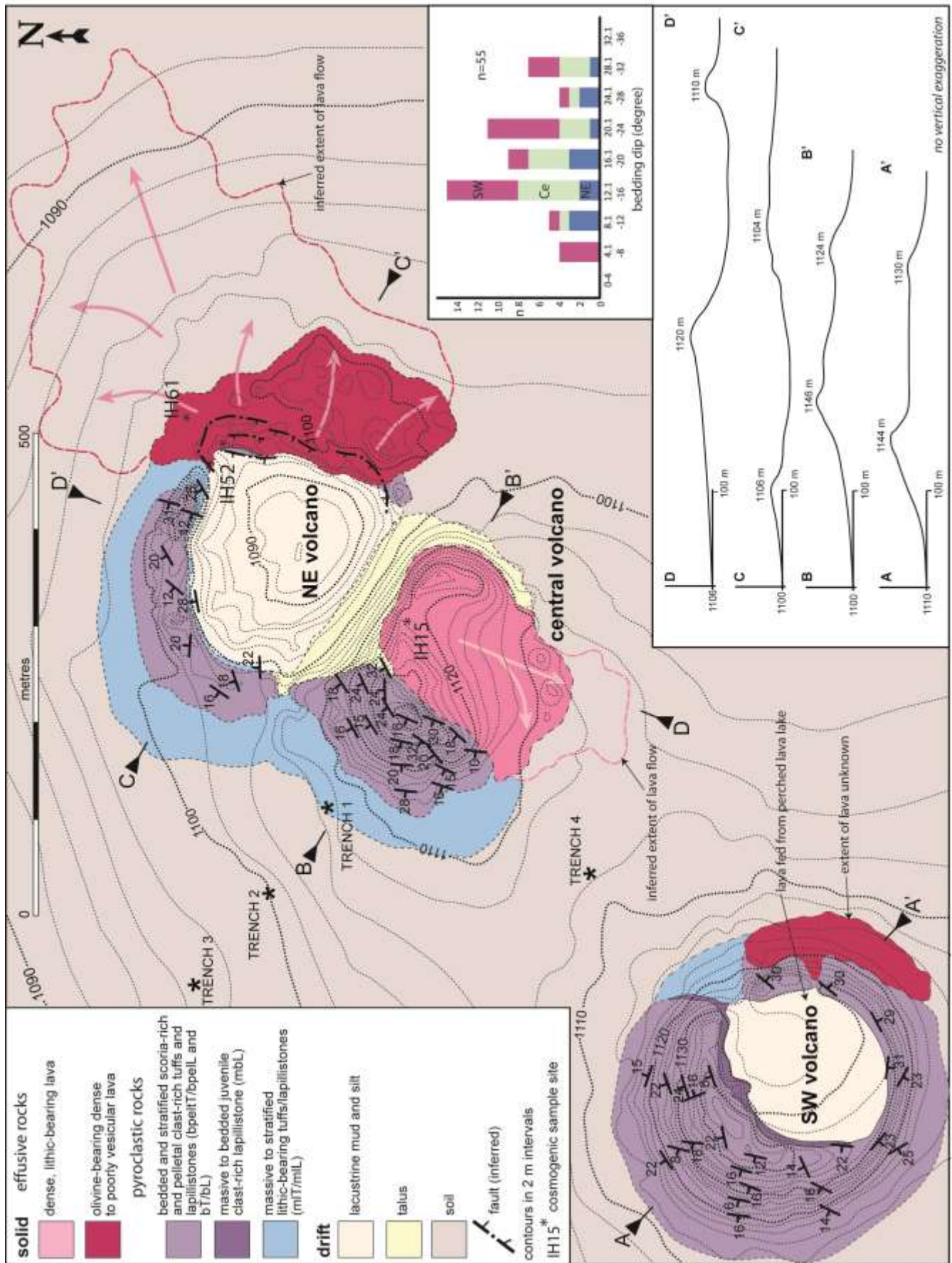
1179  
1180  
1181  
1182  
1183  
1184

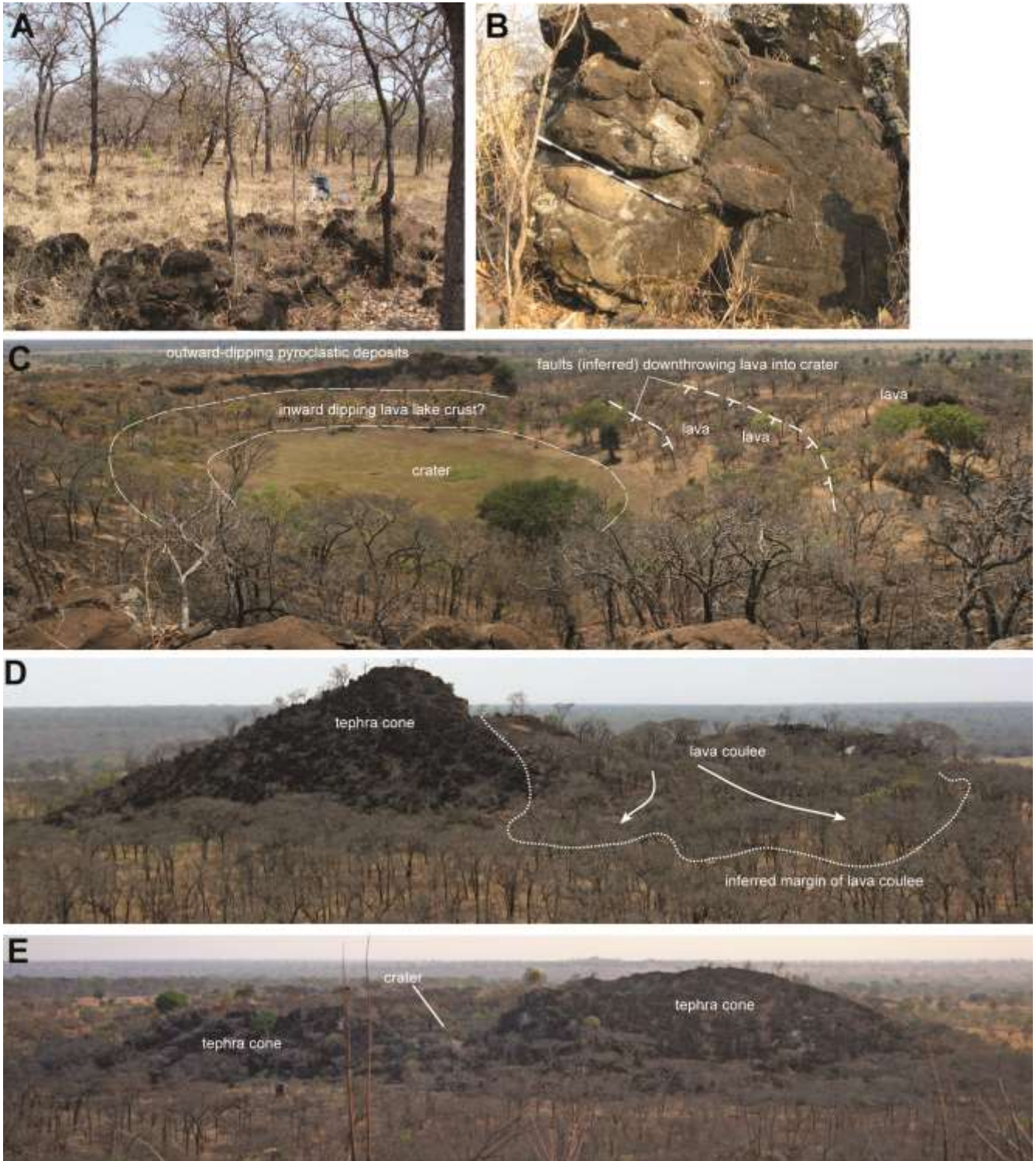
**Table 3.** Pyroclastic lithofacies of the Igwisi Hills volcanoes.



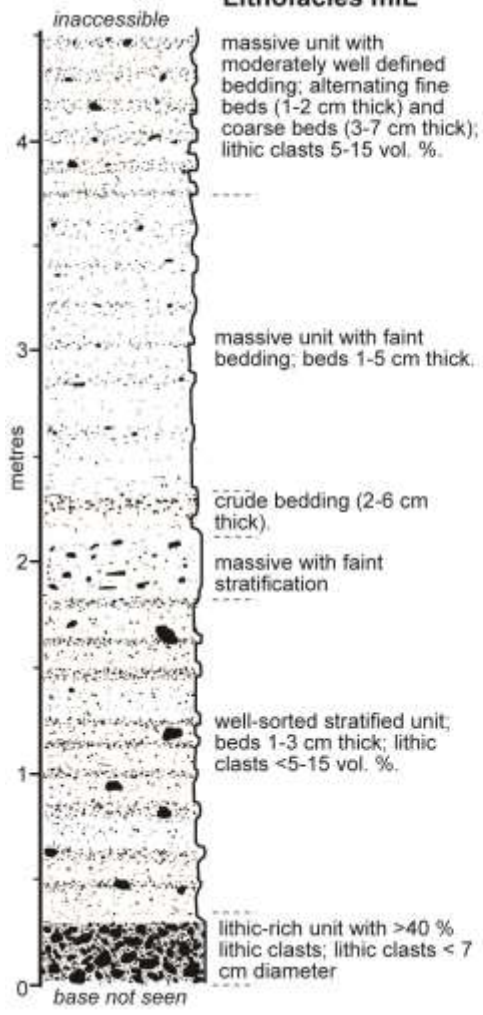
1185  
1186  
1187  
1188

1189  
1190

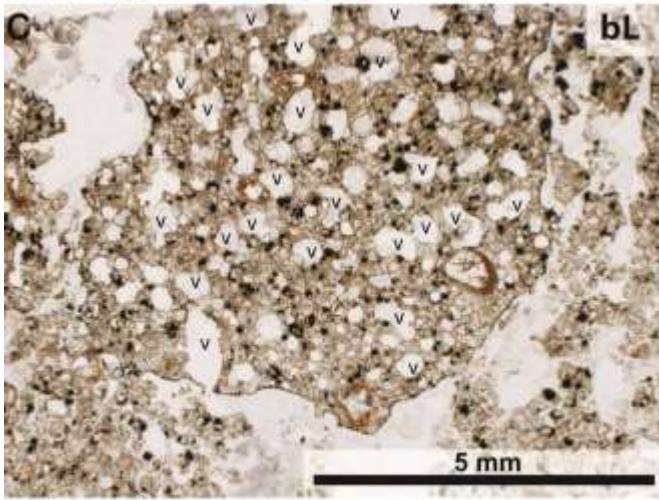
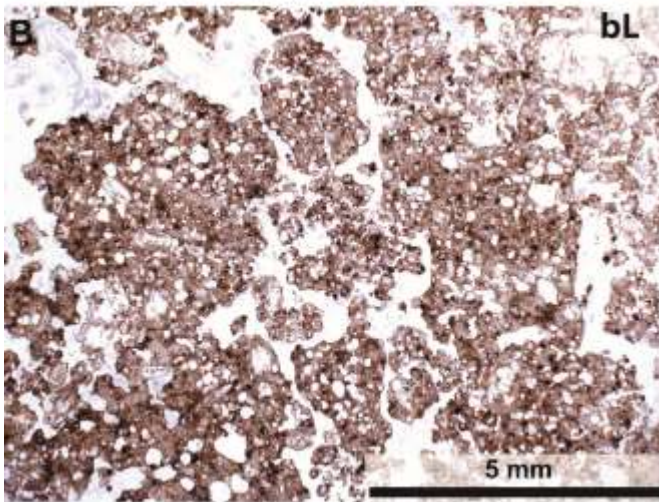
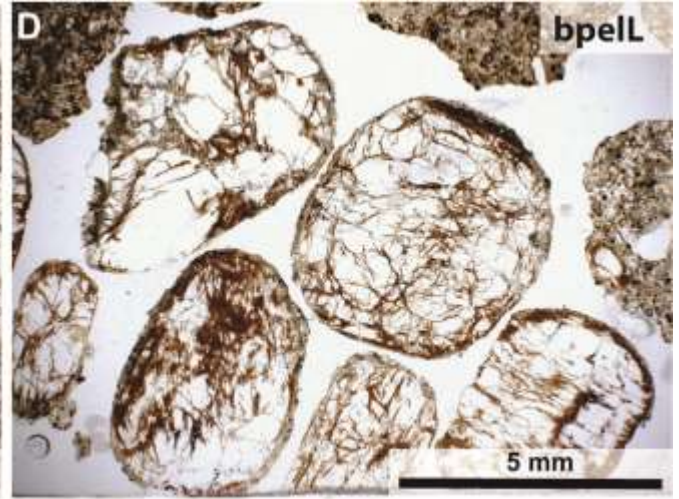
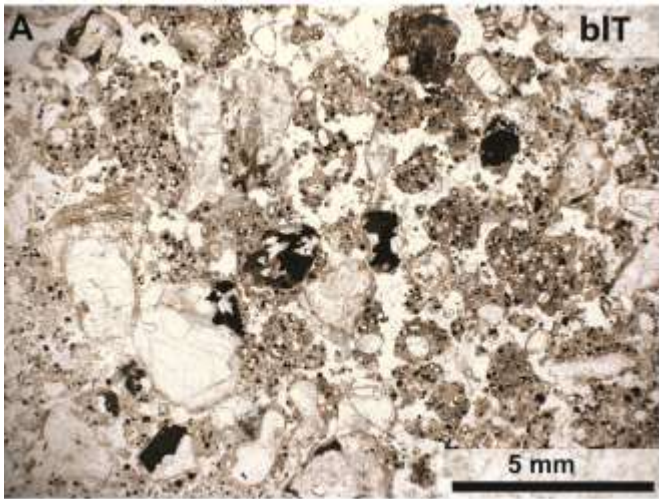




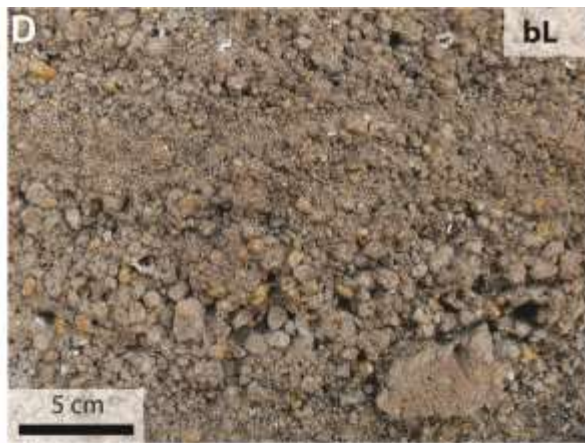
**Lithofacies mL**



1198  
1199

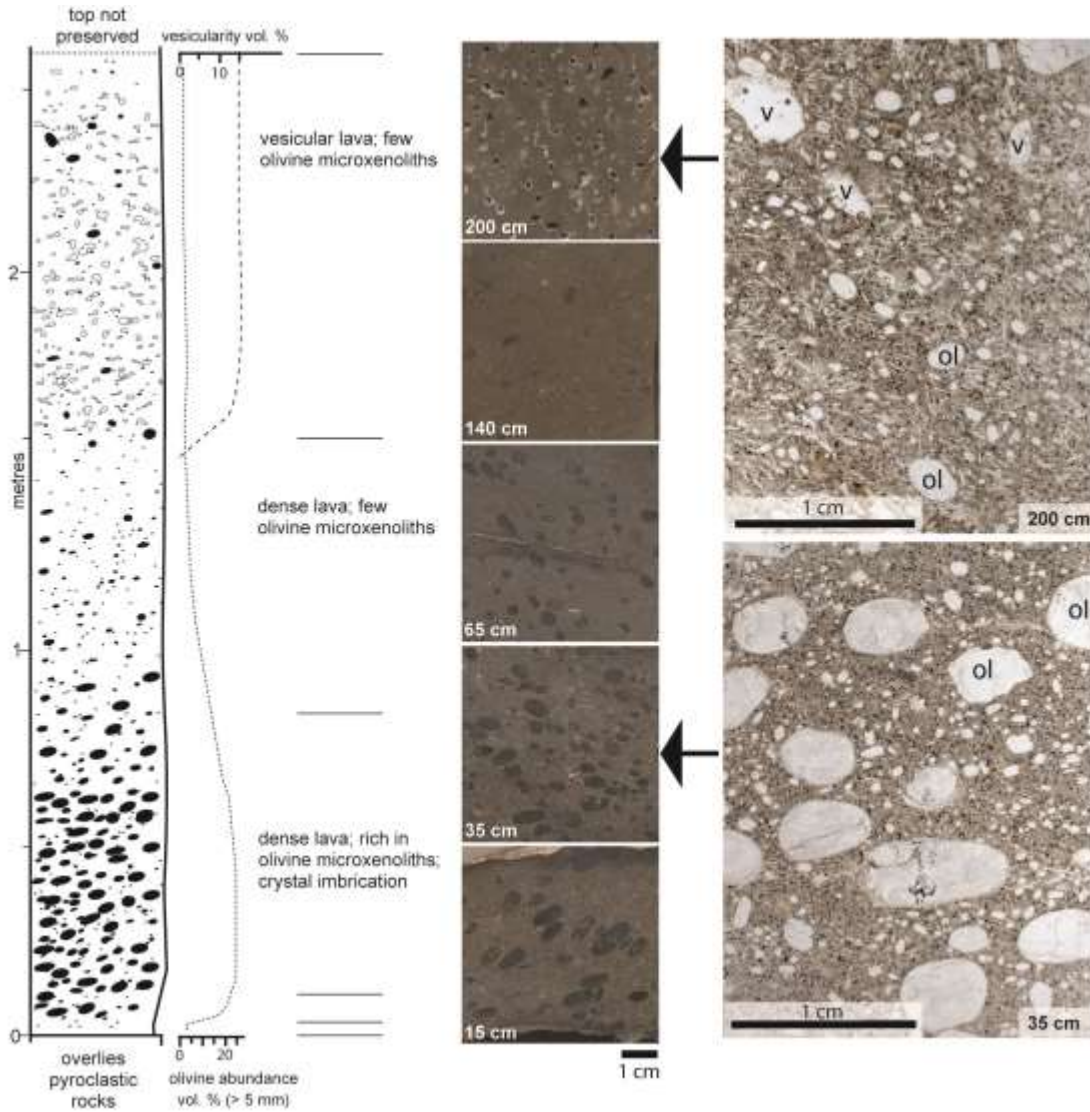


1200  
1201  
1202  
1203

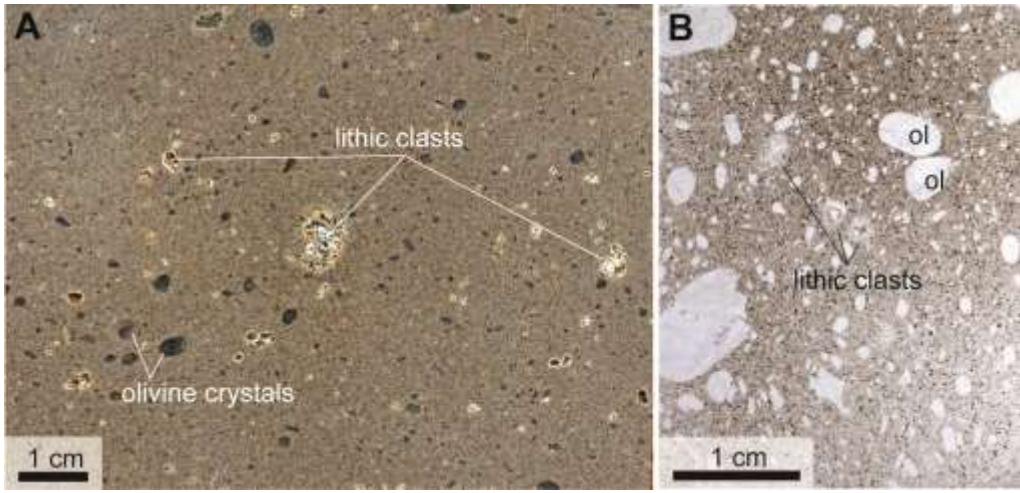


1204  
1205

1206

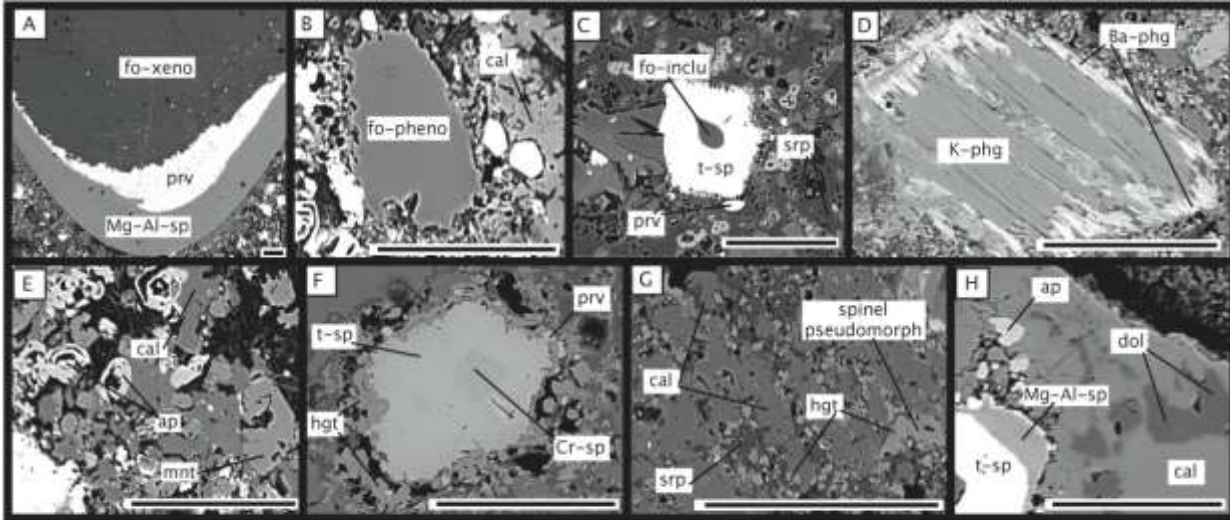


1207  
1208  
1209  
1210  
1211  
1212  
1213  
1214



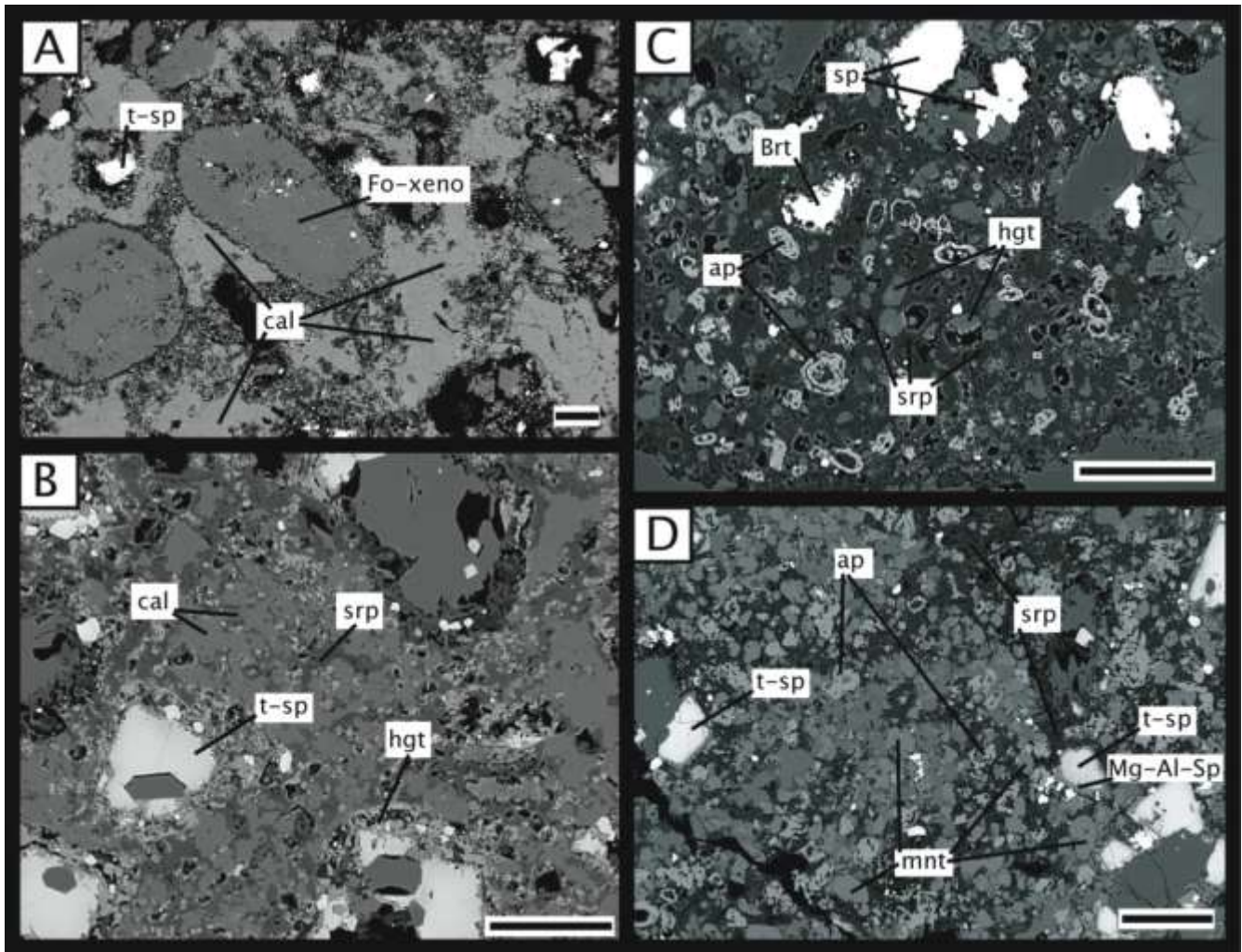
- 1215
- 1216
- 1217
- 1218
- 1219
- 1220
- 1221
- 1222
- 1223
- 1224
- 1225
- 1226
- 1227
- 1228
- 1229
- 1230
- 1231
- 1232
- 1233
- 1234
- 1235
- 1236
- 1237
- 1238
- 1239
- 1240
- 1241
- 1242
- 1243
- 1244
- 1245
- 1246
- 1247
- 1248
- 1249
- 1250

1251  
1252  
1253  
1254  
1255  
1256  
1257  
1258



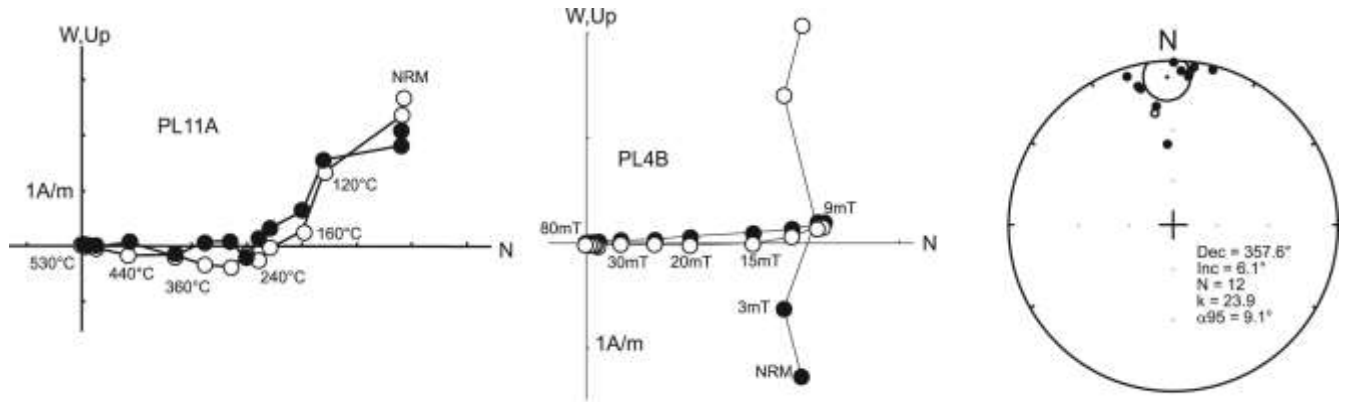
1259  
1260  
1261  
1262  
1263  
1264  
1265  
1266  
1267  
1268  
1269  
1270  
1271  
1272  
1273  
1274  
1275  
1276  
1277  
1278  
1279  
1280  
1281  
1282  
1283

1284  
1285  
1286  
1287  
1288



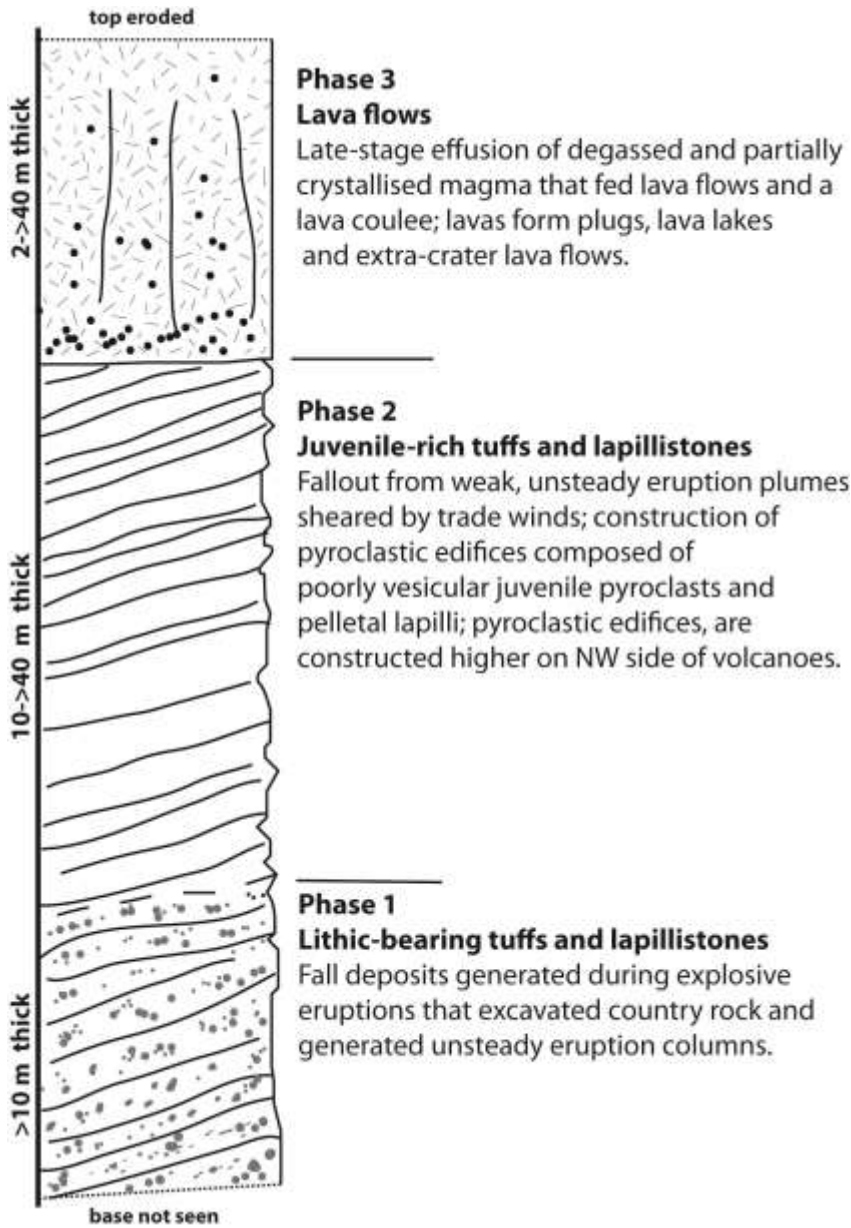
1289  
1290  
1291  
1292  
1293  
1294  
1295  
1296  
1297  
1298  
1299  
1300  
1301  
1302  
1303  
1304

1305  
1306  
1307  
1308  
1309  
1310



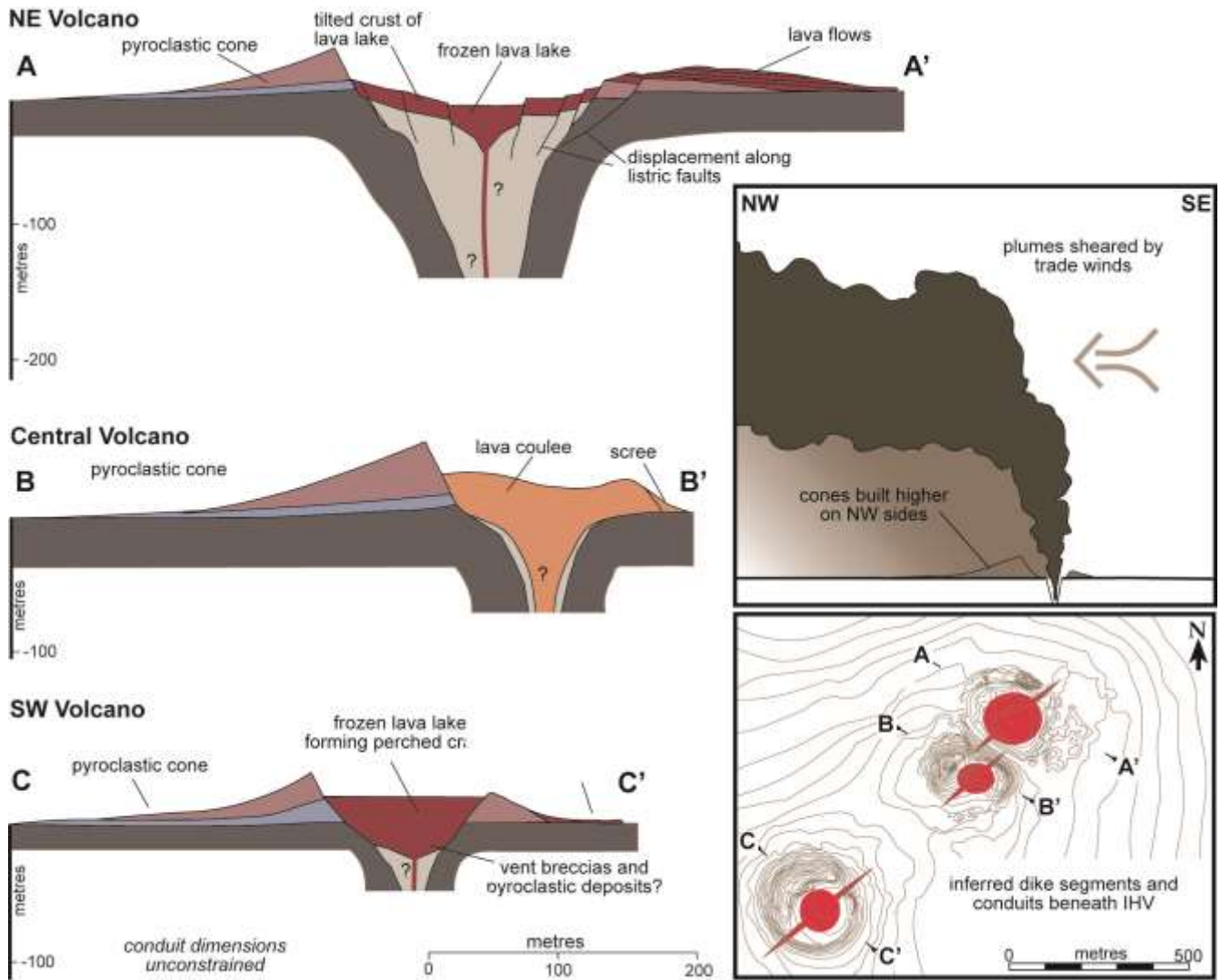
1311  
1312  
1313  
1314  
1315  
1316  
1317  
1318  
1319  
1320  
1321  
1322  
1323  
1324  
1325  
1326  
1327  
1328  
1329  
1330  
1331  
1332  
1333  
1334  
1335  
1336  
1337  
1338  
1339  
1340  
1341  
1342

1343  
1344  
1345



1346  
1347  
1348  
1349  
1350  
1351  
1352  
1353  
1354  
1355  
1356  
1357  
1358

1359  
1360  
1361  
1362  
1363



1364